CrossMark

Preatmospheric Detection of a Meter-sized Earth Impactor

David L. Clark[1,2] , Paul A. Wiegert[2,3] , Peter G. Brown[2,3] , Denis Vida[2,3] , Aren Heinze[4] , and Larry Denneau[4]

[1] Department of Earth Sciences, The University of Western Ontario, London, ON, N6A 3K7, Canada
[2] Institute for Earth and Space Exploration, The University of Western Ontario, London, ON, N6A 3K7, Canada
[3] Department of Physics and Astronomy, The University of Western Ontario, London, ON, N6A 3K7, Canada
[4] Institute for Astronomy Honolulu, HI 96822-1839, USA

Abstract

On 2020 September 18 U.S. Government (USG) sensors detected a bolide with peak bolometric magnitude of -19 over the Western Pacific. The impact was also detected by the Geostationary Lightning Mapper instrument on the GOES-17 satellite and infrasound sensors in Hawaii. The USG measurements reported a steep entry angle of $67°$ from horizontal from a radiant $13°$ east of north and an impact speed of 11.7 km s^{-1}. Interpretation of all energy yields produces a preferred energy estimate of 0.4 kt TNT, corresponding to a 23,000 kg, 3 m diameter meteoroid. A postimpact search of telescopic images found that the Asteroid Terrestrial-impact Last Alert System survey captured the object just 10 minutes prior to impact at an Earth-centered distance of nearly 11,900 km with apparent magnitude $m = 12.5$. The object appears as a $0.44°$ streak originating on the eastern edge of the image, extending one-third of the USG state-vector-based prediction of $1.26°$ over the 30 s exposure. The streak shows brightness variability consistent with small asteroid rotation. The position of Earth's shadow, the object's size, and its consistency with the reported USG state vector confirm the object is likely natural. This is the eighth preatmospheric detection of a near-Earth asteroid (NEA) impactor and the closest initial telescopic detection prior to impact. The high altitude of peak fireball brightness suggests it was a weak object comparable in many respects with 2008 TC3 (the Almahata Sitta meteorite), with an absolute magnitude $H = 32.5$ and likely low albedo. Therefore, we suggest the NEA was a C-complex asteroid.

Unified Astronomy Thesaurus concepts: Bolides (172); Sky surveys (1464); Near-Earth objects (1092)

1. Introduction

The understanding of the near-Earth asteroid (NEA) population brings with it understanding of the risks of catastrophic or locally destructive Earth-impacting events and insight into the mitigation of that risk. Fireballs are messengers of that understanding, either acting as proxies to their larger asteroidal cousins or as fragments of past asteroidal mixing. A rare and important opportunity arises when a meteoroid is observed in more than one of three regimes: in space as a meteoroid, interacting with the atmosphere as a fireball, and on the ground as meteorites. The Fireball Retrieval on Telescopic Survey Images (FROSTI) project seeks to locate serendipitous images of precontact meteoroids on sky-survey images collected for other scientific purposes (Clark 2010). We continuously collect image borehole data from a large set of sky surveys and imaging space missions; our current catalog comprises approximately 13.5 million images. As newly reported and historical fireball events become available, out of atmosphere approach trajectories for fireballs are calculated and the image catalog searched for image–trajectory intersections using a survey-independent representation of the catalog images (Clark 2014). One such source of fireball events is the Center for Near Earth Object Studies (CNEOS) Fireball web page[5] reporting on U.S. Government (USG) sensor data. In parallel and referred to by CNEOS is the Bolide Detections

from Geostationary Lightning Mapper (GLM) system (Jenniskens et al. 2018), reporting on data collected by instruments (GLM-17 and GLM-18) on board two Geostationary Operational Environment Satellite (GOES) satellites (GOES-17 and GOES-18).

Here, we report on the first successful identification by FROSTI of a preatmospheric meteoroid. The system identified that the meteoroid responsible for the USG 2020 September 18 fireball, which occurred at 08:05:25 UT over the Pacific, had potentially been imaged by the ATLAS Haleakalā Telescope (Tonry et al. 2018). The bolide was also recorded by GLM-17. Summaries of the USG and GLM bolide data can be found in Tables 1 and 2, respectively. A simulated telescopic image using the USG-reported 2020 September 18 state vector to produce an estimated trailed object, as created by FROSTI, can be seen in Figure 1. The actual Asteroid Terrestrial-impact Last Alert System (ATLAS) image, with an inset containing the trailed object linked to USG 2020 September 18, is shown in Figure 2. The capture was unusual in that the image was taken at 07:55:47 UT through 07:56:17 UT, only 10 minutes prior to the fireball. This chance timing was both fortuitous and problematic. The absolute magnitude $H = 32.5$ meteoroid was quite bright at apparent magnitude $m = 12.5$, both due to its proximity and favorable illumination just prior to entering into Earth's shadow. However, the object appears as an elongated streak originating off-image, the observed length representing only about one-third of the modeled motion of the object during the 30 s exposure. Not having the complete object path on-image reduces the amount of information available for confirmation of the object's orbit, for light-curve extraction to study the object's rotation and shape, and for predicting other sky-survey images which may contain the object.

---

[5] https://cneos.jpl.nasa.gov/fireballs/

Table 1
USG Event Description

Value Description		USG Value	Best-fit Value Δ	Δ Values for Parameter Fit Clones
Peak brightness (UT)	Date	2020 Sep 18		
	Time	08:05:27		
	Peak magnitude (bolometric)	−19		
Latitude (deg)		2.4 N	−0.1509	−0.0791 ± 0.0774
Longitude (deg)		168.7 W	0.2845	0.187 8 ± 0.0666
Altitude (km)		46.0	0.3104	2.157 7 ± 7.2171
Velocity (km s^{-1})		11.7		
Velocity (km s^{-1})	v_x	10.2	0.3855	0.272 4 ± 0.2617
	v_y	2.9	0.6807	0.689 1 ± 0.0230
	v_z	−4.9	−0.2369	−0.2102 ± 0.0362
Radiated energy from the GLM light curve (J)		5e10		
	Calculated total impact energy (kt)	0.16		
Radiated energy from the USG light curve (J)		5.6e10		
	Calculated total impact energy (kt)	0.18		
Adjusted for fireball luminous efficiency (J)		1.4e11		
	Calculated total impact energy (kt)	0.4		

Note. First two columns: the CNEOS web page entry for the 2020 September 18 USG fireball event (https://cneos.jpl.nasa.gov/fireballs/). Latitude and longitude are geodetic. Right-handed velocity components: v_z is directed along the Earth's rotational axis toward the North Pole, v_x and v_y lie on the equatorial plane, with v_x directed toward the prime meridian. The kilotons of TNT impact energy values are derived from the total radiated energy by the USG values using an empirical expression from Brown et al. (2002). The altitude here corresponds to the height of peak brightness, as does the velocity. Energy values resulting from further analysis are listed for comparison (see text). Last two columns: the change to the reported USG state vector required to best fit the candidate image streak and the USG observations. The first of these columns gives the absolute changes in values required to best fit the streak. The latter column gives the aggregate 1σ uncertainty ranges of parameter-fit clones generated from MultiNest (Feroz et al. 2011; Buchner 2016) parameter-fit covariance matrices output in the 10 runs performed, expressed as Deltas from the USG values.

Table 2
GLM Bolide Event Description

Value Description		Value
Bolide	Date/time (UT)	2020 Sep 18 08:05:25
	Latitude (deg.)	2.3
	Longitude (deg.)	−169.9
	Detected by …	GLM-17
	How found?	Algorithm
	Other detecting sources	USG
	Confidence rating	High
Signal	Start time (UT)	2020 Sep 18 08:05:25.675
	End time (UT)	2020 Sep 18 08:05:27.019
	Duration (s)	1.344
	Latitude (deg)	2.5
	Longitude (deg)	−169.9
	Total radiated energy (J)	5e10

Note. The GLM web page entry for the 2020 September 18 event (https://neo-bolide.ndc.nasa.gov/).

Figures 1 and 2 show that the predicted location of the object based on the reported USG state vector and the observed streak are on opposite sides of the 5.5° image field. This difference in position, though not unexpected for reported USG state-vector data, which is known to be of varying accuracy (Devillepoix et al. 2019), along with the truncated streak, requires that we justify the claim that the image is of the same object as the USG 2020 September 18 fireball. As we will show in Section 6, the apparent velocity of the object, its large mass (for an artificial object) together with the fact that if a preatmospheric object it is outside the Earth's shadow lead us to conclude with high confidence that the streak is the meteoroid associated with the USG fireball.

Subsequent to the image discovery, a deeper analysis of the USG and GLM data, in particular the relatively high altitude of fragmentation and the FROSTI-derived Apollo orbit of the object, have revealed some similarities of this object and the Almahata Sitta (2008 TC3) event.

At the time of publication there have been seven cases where Earth-impacting objects have been imaged in space (2008 TC3, 2014 AA, 2018 LA, 2019 MO, 2022 EB5, 2022 WJ1, and 2023 CX1). Four of these events precede the USG 20200918 fireball event. In all cases, the objects were first identified by ground-based telescopic imaging. The USG 2020 September 18 fireball event is the first case where the determination of an object's trajectory and properties have been driven by the impact event, with subsequent identification of precovery images.

2. Object Detection and Image Search

The FROSTI project (Clark 2010) searches for preatmospheric observations of meteoroids through the backwards numerical integration of the measured state vectors of fireball events and compares look angles to an ever-growing collection of sky-survey images. FROSTI's current database contains over 13.5 million image boreholes from both ground-based telescopes and spacecraft. Each fireball state vector is integrated back in time using the RADAU integrator (Everhart 1985). A 1000-clone uncertainty cloud is generated for each event based on state-vector uncertainties. In cases where multiple trajectory or physical models lead to differing state vectors, each model is treated as a separate event. Results from
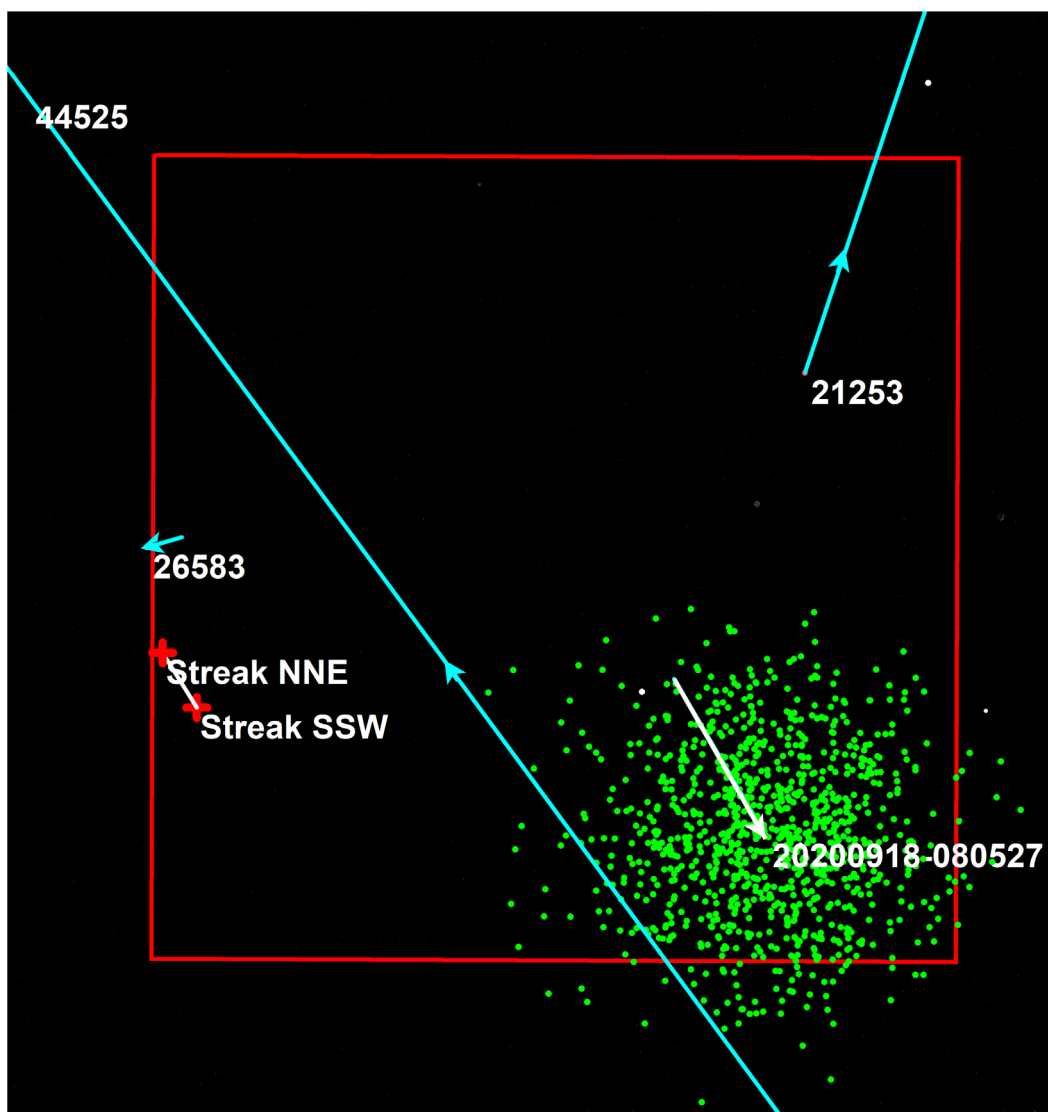
Figure 1. A simulation of ATLAS image 02a59110o0264c showing the predicted path of the USG fireball on the image based on a trajectory integration backward in time from the meteoroid contact state reported by the USG. The white arrow represents the predicted motion of the nominal object between the start and end of the exposure. Green dots represent the end of exposure positions of 1000 clones generated using standard deviations of 0.1°, 0.1 km, and 0.1 km s^{-1} on the USG-reported values. The position of the the actual image streak is shown in white at the left between its north-northeast and south-southwest endpoints. Shown in blue are the paths of the three cataloged satellites that crossed the field of view of the image, object 26583, appearing in the actual image in Figure 2, and objects 21253 and 44525, which were in the Earth's shadow and not imaged. Note the image size is 5.5° on a side.

all such fireball scenarios and images yield a list of potential precovery images that are then prioritized for manual visual inspection based on a predicted object's apparent magnitude, the portion of the uncertainty cloud on a given image, and the limiting magnitude of the image in question. From over a decade of FROSTI monitoring the 94% probability of an 11.5 mag USG fireball of 2020 September 18 appearing on ATLAS 1 image 02a59110o0264c, taken 10 minutes prior to the fireball event, was exceptional (see Figure 1 for the simulated image capture). Based on the nominal USG contact state vector, the preimpact meteoroid should have been seen as a 4519″ long streak on the east (right) side of the image. Later measurement of the actual streak resulted in a visual magnitude of 12.5, very similar to FROSTI's prediction.

Tables 1 and 2 summarize the bolide as reported by USG and GLM. Slight differences in the impact locations between USG and GLM are due to GLM's assumed (and fixed) height

of 16 km near the equator (Jenniskens et al. 2018). The GLM light curve produced excellent agreement in total radiated energy with the USG value, being only 10% less than that recorded by the USG.

In general, FROSTI determines object visibility on an image from a calculated object size expressed by diameter or absolute magnitude. The estimated visibility of a USG-reported object is arrived at by calculating kinetic energy from impact energy using the formula documented on the CNEOS Fireballs Introduction web page,[6] converting to a mass and diameter assuming a bulk density of 3000 kg m^{-3}, and using the standard absolute magnitude methodology of Bowell et al. (1989). For the initial search, this produced an initial estimate of mass $M = 8600$ kg, diameter $d = 1.8$ m, and absolute magnitude $H = 31.5$. Measurement of the image streak and
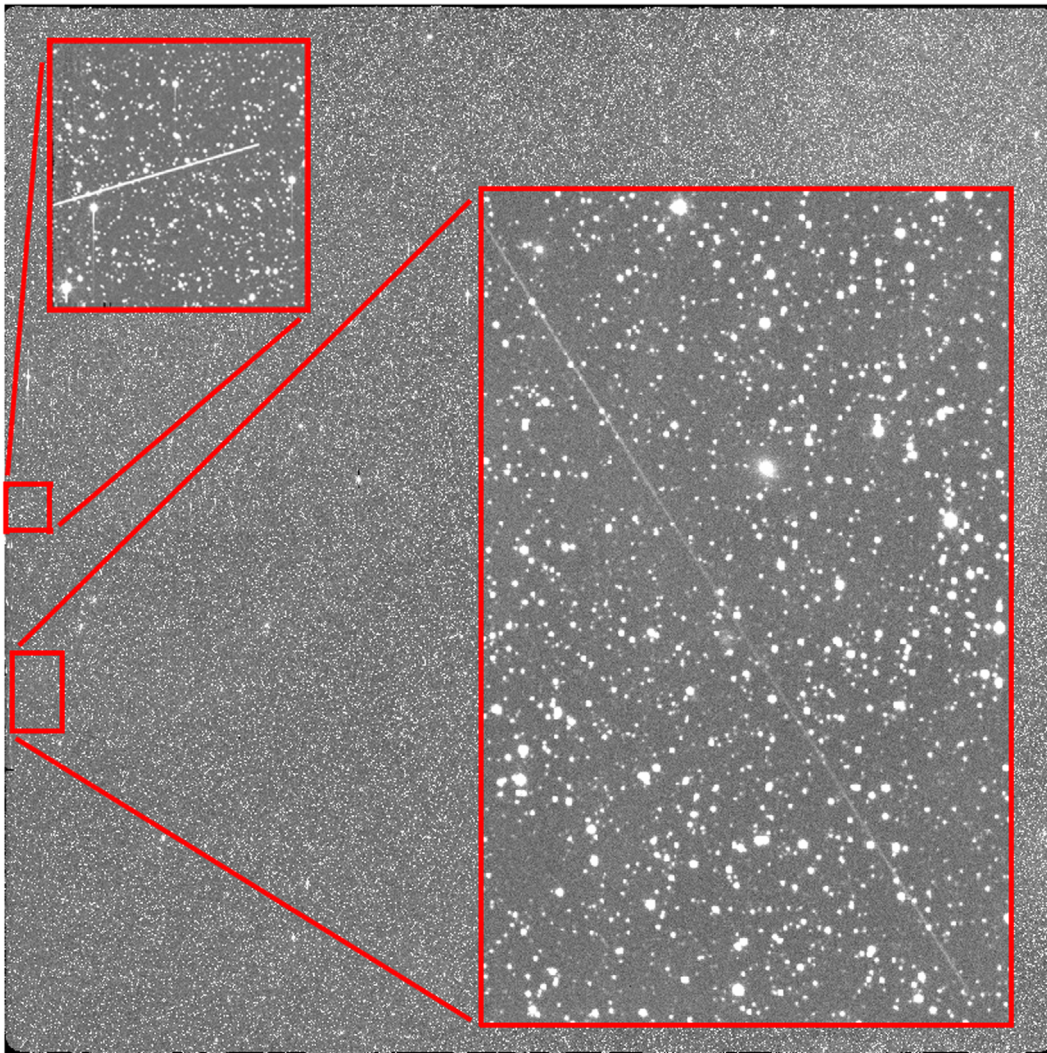
---

6   https://cneos.jpl.nasa.gov/fireballs/intro.html

Figure 2. ATLAS image 02a59110o0264c, with cutouts showing the location of the USG 20200918 object streak (right) and the Kosmos 2319 SL-12 rocket body, both at the eastern (left) edge of the image.

interpretation of the GLM and USG light curves applying more physical luminous efficiency values at low entry speeds (described in Section 3.2) produced a final best estimate of the object as having $H = 32.5$. This refined and fainter absolute magnitude actually corresponds to higher diameter and mass based on an assumed lower bulk density (similar to 2008 TC3), resulting in a correspondingly lower albedo than usually assumed by FROSTI.

Back-integration of the contact state vector and uncertainties for a period of 2 months yields the pre-Earth encounter orbit given in Table 5 and shown in Figure 3. The meteoroid was in an Apollo orbit with Earth impact occurring on the inward leg of the object's orbit, making its approach a nighttime one favorable for telescopic observation. The near-Earth–like orbit resulted in a low Earth-relative velocity at encounter.

The FROSTI image-search system generates simulations of object–image intersections, an example of which can be seen in Figure 1, and a large amount of nominal object and uncertainty clone motion information, highlights of which can be found in Table 4. The expected scenario in developing the search system was that that there would be a set of similarly pointed images, all or most of which would contain an object at varying positions. The nominal object and uncertainty clone motion analysis would be performed across the set of images, with manual image blinking or automated object searching then being performed, much as typical near-Earth object (NEO) detection proceeds. However, in the case of this object, where the epoch of the capturing image is just 10 minutes prior to object impact, the on-image motion of the object is immense ($4519''$ or $1.25°$ in 30 s). The image was part of a quartet, but with such extreme motion the meteoroid was outside the fields of the other quartet images. The initial image search was performed with the standard 1000-clone uncertainty cloud, with the search result indicating that the object had a 99.9% probability of being on the image at the beginning of the exposure and a 93% probability at the end. The object was predicted to appear as a streak on the east (right) side of the image extending in a south-southwest direction.

The USG reports do not include uncertainties in position and velocity, so as a default we use standard deviations of one reported decimal place on each state element ($0.1°$, 0.1 km, and 0.1 km s^{-1}) and a standard deviation of 1.0 s on the reported contact time to determine on-image probability. Using the standard calculation for apparent magnitude m as documented

Table 3
Assumed and Derived Meteoroid Properties

Property Description		Original		Refined
Total radiated energy (J)	Observed	4.1E10	Observed	1.4E11
Impact energy (kt)	Derived	0.14	Derived	0.4
Velocity (km s^{-1})	Observed	11.7	Observed	Same
Mass (kg)	Derived	8600	Derived	23,000
Absolute magnitude (H)	Derived	31.5	Derived	32.5
Density (kg m^{-3})	Assumed	3000	Derived	1660
Diameter (m)	Derived	1.8	Derived	3
Albedo	Assumed	0.15	Derived	0.02
Slope parameter	Assumed	0.15	Assumed	Same

Note. Summary of the derived versus directly observed object attributes. These were used both for calculating on-image object appearance and in determining if the object was natural or man-made. The original USG total radiated energy was used for estimating the object mass and therefore diameter in the original FROSTI image search. The standard FROSTI bulk density of 3000 kg m^{-3} and albedo of 0.15 were used. Post analysis, including the GLM and infrasound observations together with revised luminous efficiency and similarity to 2008 TC3, yields a best-estimate threefold greater mass. Analysis of the presumed object streak's light curve revealed that initial FROSTI magnitude estimates were one magnitude too bright. High-altitude fragmentation is consistent with a much lower bulk density. A very low albedo is required in order to enforce consistency of the derived diameter and the apparent magnitude.

in Bowell et al. (1989) and an assumed phase-angle slope parameter (G) of 0.15, we calculate $m = 12.4$, representing an unusually bright candidate for detection. However, the extreme on-image motion was expected to introduce substantial trailing loss, estimated to be on the order of nine magnitudes.

USG fireball reports have been found to have large uncertainties in velocity (Brown et al. 2015; Devillepoix et al. 2019). To address the possibility that the chosen uncertainties of the USG-reported values may be too small and may have disqualified other images potentially containing the object, we performed an additional image search with the standard deviation expanded threefold to identify any images competitive with the proposed capture image. The proposed capture image–object intersection probability was reduced to 78%, not unexpectedly, but the new uncertainty cloud did now incorporate the candidate streak. Only one additional image was found with an object intersection probability greater than 5% at a time when the object would have been brighter than an image's limiting magnitude and no streak was visible on that image.

Figure 2 gives the actual ATLAS 1 image 02a59110o0264c. The image is centered on R.A. $20^h6^m30^s$ and decl. $8°10'41''$. The image field is approximately 5.5° per side, with celestial north up and celestial east to the right. Visual inspection of the image revealed an illuminated $1590''$ (0.44°) streak, one end located at the west (left) edge of the image, the other end on-image (see Figure 2, inset); it appears almost exactly 4° east of the predicted position and 0.9° to the south. The streak's slope is only 2.1° steeper than predicted. The overall length of the streak and its direction of travel (south-southwest or north-northeast) cannot be determined from the image alone. A comparison of the predicted position of the streak from FROSTI as compared to the observed is provided in Table 6.

The 4° offset between the predicted object position and the imaged position highlights that it was fortuitous the manual image identification was made. A small offset in USG contact

state or in the actual orbit of the object could have resulted in the position difference being more than one field of view, substantially lessening the chance the image would have been identified and the event investigated. The position difference also highlights that the physical object could possibly appear on other as-yet-unidentified images which did not contain the FROSTI-predicted object.

3. Fireball Properties

As the impact occurred over open ocean, all data available for the associated fireball are from three sources: USG sensors,[7] the GLM on board the GOES-17 satellite stationed over the Pacific, and an infrasound array located in Hawaii.

3.1. Energy

Infrasound (low-frequency sound) from the bolide was detected at the IS59US array in Hawaii at a range of 2400 km beginning just after 10:20:00 UT, as shown in Figure 4. Using the approach in Ens et al. (2012), all four array elements were stacked from the apparent direction of the air-wave arrival to find a period at maximum amplitude from zero crossings (see ReVelle 1997) of 4.1 ± 0.3 s. Using the progressive multi-channel correlator approach of Cansi (1995), we derive a period of 3.7 ± 0.6 s, in agreement within uncertainty. The beamformed max pressure signal amplitude is 0.05 Pa using a bandpass from 0.1 to 2 Hz.

Taking this period at maximum amplitude and the single station empirical yield–period relationship for bolides from Ens et al. (2012), we estimate a nominal source yield of 0.6 kt TNT equivalent, but with an uncertainty range of [0.2, 0.7] kt. Using the bolide–amplitude yield relations in Ens et al. (2012) and a computed stratospheric wind index of $6.7 \, \mathrm{m \, s^{-1}}$ from the ECMWF atmosphere model from source to IS59US, we derive a wind-corrected yield of 0.35 kt.

Taken together, the available infrasound records suggest an energy in the 0.3–0.6 kt range as most probable.

The published USG data (see Table 5) include the event time, location, velocity, height of peak brightness, and total radiated energy together with a light curve of radiant intensity as a function of time. The latter can be used to estimate the total impact energy based on cross calibrations for events simultaneously detected by other techniques (infrasound, meteorite recoveries, ground-based optical measurements; Brown et al. 2002; Edwards et al. 2006). Among these USG sensor-measured metrics, the radiant direction and to a lesser extent speed have been shown to be the least accurate quantities through comparison with high-precision, ground-based trajectory measurements, while the height of peak brightness has tended to be more accurate, with typical errors being 3 km (Borovička et al. 2015; Brown et al. 2015; Devillepoix et al. 2019). The fireball location and energy are typically most secure, the former being more limited by the published precision.

For the USG energy, we can compare to the GLM-derived energy. Here, we follow the procedure outlined in Jenniskens et al. (2018), where the total energy in the GLM bolide light curve is summed, range-corrected, and a 6000 K blackbody spectrum assumed. Under these assumptions, a total optical energy of 5×10^{10} J is found from the GLM light curve, in
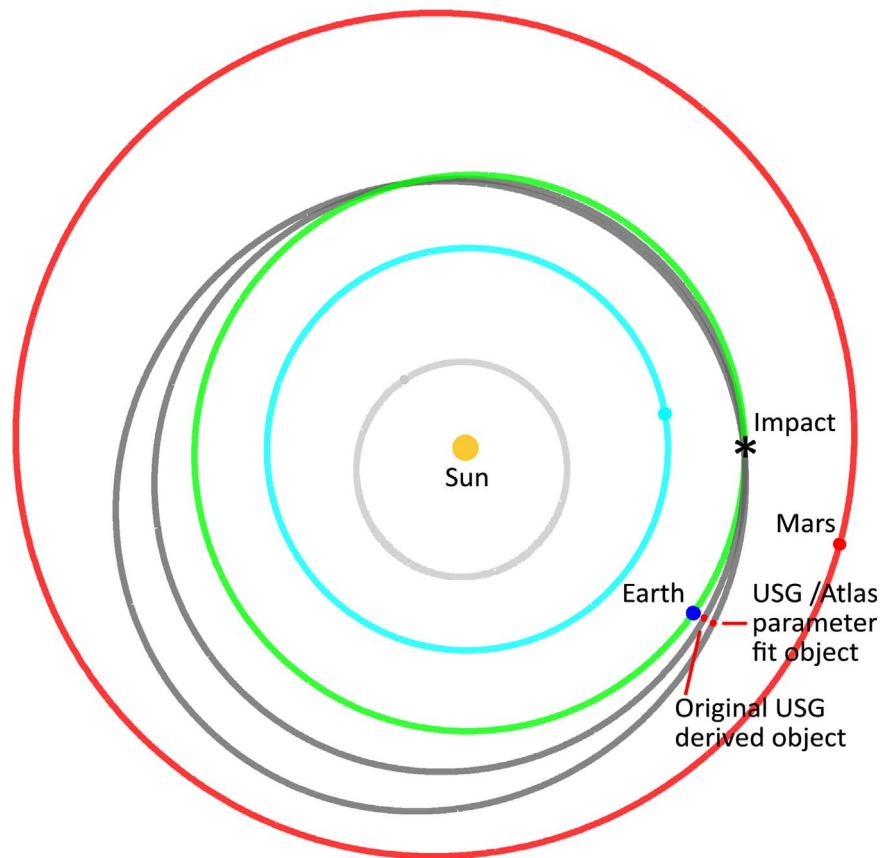

Figure 3. Illustration of the meteoroid's Apollo Earth-crossing orbit. The inner meteoroid orbit is that derived directly by FROSTI from the USG event for use in the search for precovery images. The outer orbit is the refined orbit computed from the best-fit trajectory using both the USG observation and the object streak on the ATLAS image. The planets and meteoroids are positioned 1 month prior to the fireball event. The impact point of Earth and the meteoroid is marked with the asterisk.

Table 4
Image and Predicted Object Appearance

Description	Value
Sky survey	ATLAS 1
Image ID	02a59110o0264c
Start time (UT)	2020 Sep 18 07:55:47
End time (UT)	2020 Sep 18 07:56:17
R.A.	$20^h6^m30\overset{s}{.}730$
decl.	$8° 10'41\overset{''}{.}520$
Exposure (s)	30
On-image probability (start)	99.9%
On-image probability (end)	93.1%
On-image motion (arcsec)	4519.2
Phase angle (deg)	55.8
Apparent magnitude (m)	12.4
Trailing loss (magnitudes)	9.1

Note. The on-image probabilities are based on a 1000-clone uncertainty cloud gravitationally integrated from a set of contact states, being the mean USG-reported state with standard deviations of one reported decimal place on each state element (0.1°, 0.1 km, and 0.1 km s^{-1}). A standard deviation of 1.0 s is used over the USG-reported impact time.

good agreement with the 5.6×10^{10} J we derive from integration of the original light curve from USG sensors. From the light-curve maximum radiant intensity, the peak bolometric magnitude of the fireball was −19.

The resulting total radiated energy can then be converted to a total energy using an estimate for the luminous efficiency (η). The standard approach is to use the averaged relation from Brown et al. (2002), which yields an energy of 0.18 kt and $\eta = 0.07$. This is 2–3 times lower than the infrasound yield estimates using either amplitude or period. As the generic relation derived by Brown et al. (2002) was based on a collection of bolides having an average speed near 18 km s^{-1}, substantially above the 12 km s^{-1} for the current case, it is probable the real luminous efficiency is lower than the average value given in Brown et al. (2002).

Borovička et al. (2020) has proposed the most robust fireball luminous efficiency relation to date, using the velocity dependence proposed by ReVelle & Ceplecha (2001) and validated through modeling of meteorite-producing fireballs where material is recovered on the ground. Using that formalism, we expect a factor of ≈2 higher value for fireball luminous efficiency at 18 km s^{-1} compared to 12 km s^{-1}. Adopting this change for η produces an energy estimate of 0.36 kt TNT and agreement between both optical estimates and the infrasound energy estimates within uncertainty. We suggest that the most likely energy for the event was close to 0.4 kt TNT on this basis.

3.2. Physical Characteristics

From these data alone, we can place this event in some physical context. Figure 6 shows the height at peak brightness for all meter-sized Earth impactors published to date. The majority of these are from the CNEOS-JPL site, but half a dozen (black squares) are the height of peak brightness from fireballs which produced meteorites (Brown et al. 2015; Borovička et al. 2021; Jenniskens et al. 2021).
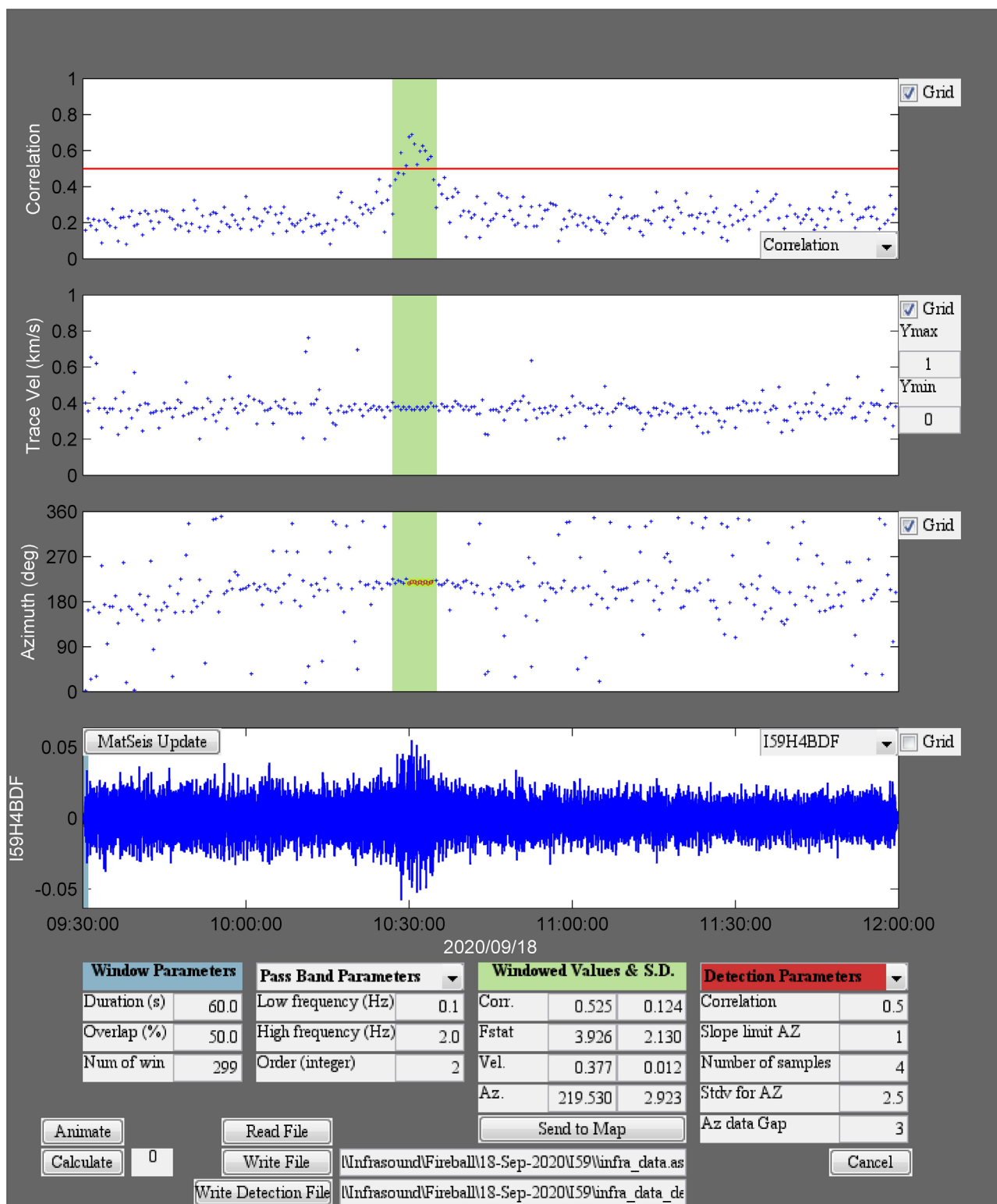
Figure 4. Infrasound detected at the four-element IS59 array in Hawaii from the USG 20200918 bolide. The bolide signal is centered around 10:30:00 UTC. Shown is the bandpassed waveform between 0.1 and 2 Hz (bottom plot) in units of pascals for element 4 of the array. Here, we have used 60 s windows with 50% overlap and found the best beam correlation (top plot), array trace velocity (second from top), and apparent back azimuth (third plot from top). The main air-wave arrival is highlighted by the vertical green bar. From I59 the great circle back azimuth to the USG fireball location is 218°, while the average observed back azimuth of the signal across all frequencies centered at 10:30:00 UT is $219.5 \pm 2.9°$.

In general, a fireball's peak brightness is reached well after the first fragmentation episode, implying that the dynamic pressure at the height of peak brightness is an upper limit to the global strength of the object. Most meteorite-producing fireballs have global compressive strengths of order 1 MPa (Popova et al. 2011; Brown et al. 2015), but reach the point of peak brightness when dynamic pressure is several times this value.

Table 5
Orbital Elements

Element	Element Description	USG	Best Fit
a	Semimajor axis (au)	1.077 ± 0.013	1.117 ± 0.034
$1/a$	Semimajor axis reciprocal (au^{-1})	0.930 ± 0.011	0.896 ± 0.027
q	Perihelion (au)	0.965 ± 0.002	0.948 ± 0.003
Q	Aphelion (au)	1.189 ± 0.028	1.285 ± 0.071
e	Eccentricity	0.103 ± 0.012	0.150 ± 0.028
i	Inclination (deg)	4.968 ± 0.463	6.530 ± 0.787
Ω	Longitude of ascending node (deg)	176.15 ± 0.16	175.843 ± 0.197
ω	Argument of perihelion (deg)	234.52 ± 2.32	236.145 ± 4.026
f	True anomaly (deg)	-110.18 ± 2.62	-110.108 ± 4.618
M	Mean anomaly (deg)	261.23 ± 4.05	266.663 ± 8.073
Tp	Time at perihelion (TD)	2020 Nov 9 06:39:16	2020 Nov 8 16:46:49
	$\pm$ (in days)	± 2.612	± 4.586
Tj	Tisserand's parameter	5.7 ± 0.05	5.574 ± 0.131
	Epoch (TD)	2020 Jul 20 08:06:36	2020 Jul 20 08:06:36

Note. USG: orbital elements of the object determined by back-integrating the reported USG contact state in Table 1 for 2 months, using an uncertainty cloud of one significant digit in the state-vector components as standard deviation (0.1°, 0.1 km, and 0.1 km s^{-1}). Best Fit: orbital elements determined by back-integrating the 20,000 clones produced by 10 parameter fitting runs finding the best self-consistent match of the on-image streak and USG observations as described in Section 5.

As every fireball fragments differently depending on its collisonal history, entry models can at best capture only a rough correspondence of expected height of peak brightness as a function of global compressive strength, under the assumption of some standard fragmentation model. Here, we use the triggered progressive fragmentation model (TPFM) described by ReVelle (2006). Ceplecha & McCrosky (1976) showed that fireballs can be approximately divided into four groups (I, II, IIIa, IIIb) progressing from strongest to weakest. These have been tentatively associated with stronger (ordinary chondrite) meteorites, carbonaceous chondrites, and weak (and weaker) cometary-like material, respectively (Ceplecha et al. 1998). Using this categorization, ReVelle (2002) adopted compressive strengths within the TPFM framework at which these various classes on average first fragment in the atmosphere, progressing from 0.7 MPa for Type I fireballs, to 0.2 MPa for Type II, 0.01 MPa for Type IIIa, and 0.001 MPa for Type IIIb.

Using these values for strength and a representative energy of 0.4 kt for a typical impactor from the CNEOS-JPL data set (Brown et al. 2015), the TPFM estimates for the expected height of peak brightness by fireball type as a function of entry speed are shown in Figure 6 (blue lines).

Notably, most of the fireball-producing meteorites fall in either the Type I or Type II category, as expected. Among the best comparator event for USG 20200918 is the Almahata Sitta meteorite fall (Jenniskens et al. 2009). This meteorite was produced from the impact of 2008 TC3, which entered at a very similar speed as USG 20200918. It was the first preatmospheric asteroid impactor imaged telescopically. It entered at a much shallower entry angle than USG 20200918 and was several times more massive (Borovička & Charvát 2009), and produced an extended series of flares near 40 km. The 2008 TC3 fireball fragmented under just a few tenths of megapascals pressure, providing clear evidence of the very weak nature of the Almahata Sitta meteoroid, which subsequent analyses using multiple techniques established as a probable rubble-pile assemblage with roughly 50% porosity (Borovička & Charvát 2009; Welten et al. 2010; Kohout et al. 2011) and an estimated bulk density of 1660 kg m^3 (Welten et al. 2010).

Given the higher height of peak brightness for USG 20200918 and even lower speed than Almahata Sitta, it is probable that it was similarly weak. Presuming its earliest fragmentation occurred 10–20 km above its height of peak brightness, as suggested by the TPFM modeling—for comparison, Almahata Sitta showed evidence for fragmentation as high as 53 km (Borovička & Charvát 2009), some 16 km above its point of peak brightness—suggests a global strength $\leqslant 0.1$ MPa. This would place the meteoroid in the C or possibly D low-strength meteoroid categories of Borovička et al. (2020) and be consistent with either a rubble-pile assemblage, collisionally reassembled material, or its having very high microporosity.

The other three meteorite-producing fireballs from meter-sized or larger objects that show a height of peak brightness at comparable dynamic pressures to USG 20200918 near the 1 MPa line are Kosice (H5 ordinary chondrite; Borovička et al. 2013), Flensberg (C1-ungrouped; Borovička et al. 2021), and Sutter's Mill (CM2; Jenniskens et al. 2012). The weakness of the two carbonaceous chondrites is as expected given their material properties. Kosice was shown to be an unusually weak meteoroid for an H5 chondrite fall, fragmenting initially under a dynamic pressure of only 0.1 MPa (Borovička et al. 2013).

To model the fireball in more detail, we attempt to match the GLM and USG light curves using the semiempirical fireball ablation model of Borovička et al. (2013, 2020). We fix the initial mass at 23,000 kg (corresponding to our preferred energy of 0.4 kt) and an initial speed of 12.7 km s^{-1} (see next section). We assume $\Gamma A = 1.21$, an ablation coefficient of 0.08 s^2 km^{-2}, and then generate a synthetic light curve using the luminous efficiency model of Borovička et al. (2020). Note that the resulting fit is not unique but representative of a family of possible fragmentation solutions. This is particularly the case as we have no detailed dynamics to simultaneously fit.

Our resulting fit is shown in Figure 5. The main feature of the light curve is the two prominent maxima separated by almost 10 km in height. We find that the first maximum can be reproduced assuming release of half a dozen fragments each of order a tonne in mass which erode (release grains) rapidly in the early flare. These initial boulders are released under an extremely low dynamical pressure of 0.1 MPa.

The second flare can be matched assuming release at dynamical pressures of 0.3 MPa of another four multi-tonne masses which erode even faster than the first set.
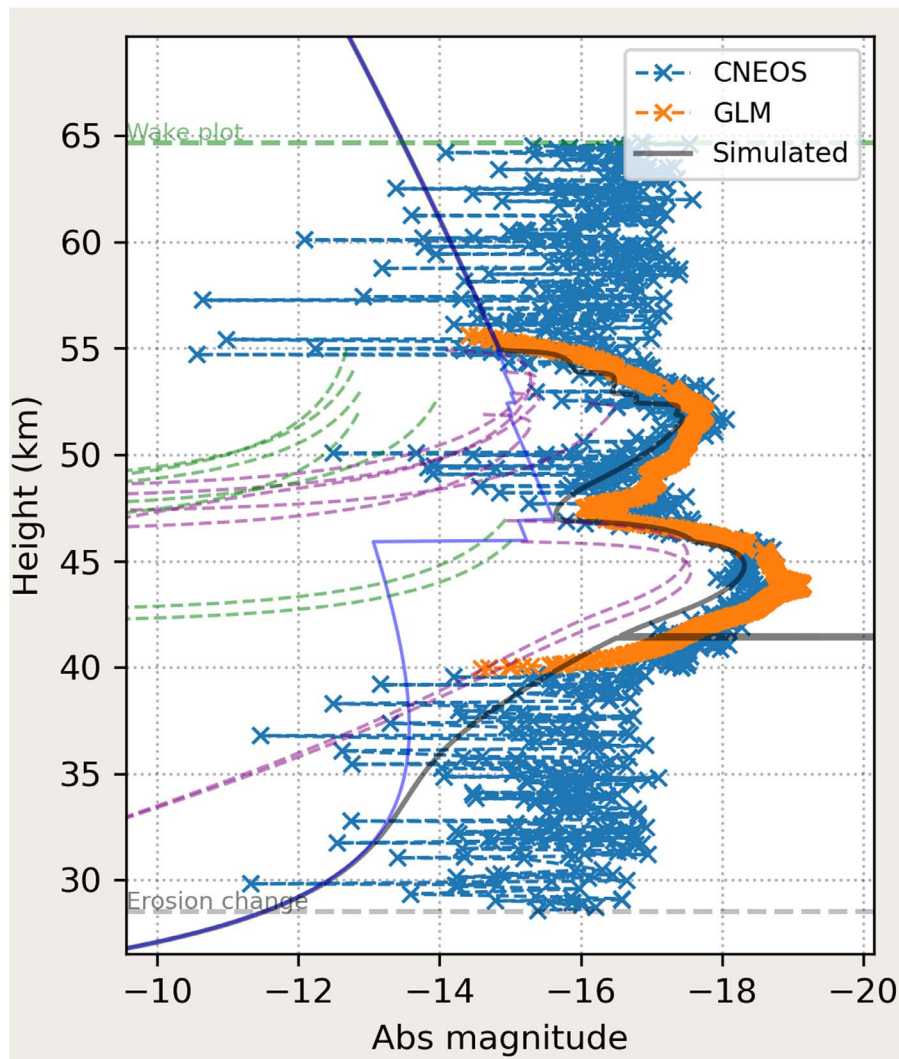
Figure 5. The observed fireball light curve as a function of height as measured by USG sensors (blue) and by the GLM instrument (orange). The GLM light curve has been computed assuming a 6000 K blackbody following the procedure of Jenniskens et al. (2018). Also shown is the light-curve model fit (see text for details). Individual fragment light curves are shown as green hatched lines, associated dust released as erosion as purple hatched lines, and the main fragment light curve is shown as a blue solid line.

These fragmentation episodes are most consistent with the weaker strength classes defined by Borovička et al. (2020), namely class C (or the very weak end of class B) objects. In the Borovicka classification, class C objects are interpreted as being loosely bound material which has reassembled following catastrophic collisions. These could resemble weak macroscopic fragments loosely bound in a rubble-pile formation but lacking significant interstitial dust.

Thus, the overall picture which emerges for USG 20200918 is of a weakly bound object of 3 m diameter on an Earth-like orbit. We note that, among the USG-reported meter-sized objects, there is a peculiar population of four other very weak objects that impact Earth at low speed (and have Earth-like orbits), which occur just above USG 20200918 in Figure 6. Why these do not occur at higher speeds is unclear. We do note that in order to reconcile the 3 m diameter with the magnitude $H = 32.5$ determined from the light curve in Section 4 that an extremely low albedo of approximately 0.02 must be used. We discuss this further below. A summary of proposed object properties is provided in Table 3.

4. Telescopic Light Curve of the ATLAS Detection

The light curve seen by ATLAS is shown in Figure 7. It is extracted from the difference image computed by subtracting from the original image a low-noise stack of prior images convolved to the point-spread function of the original image (Heinze et al. 2018). With this method of image subtraction the original image's photometric calibration and noise properties are preserved. Though stars are largely removed by the differencing process, some artifacts remain. As a result, all portions of the trail which are less than 8 pixels from the centroid of a star are masked out. The remaining portion of the trail (which is 1582″ long, corresponding to 10.7 s of time, assuming our calculated average rate of motion of 148″ per second) is sampled with 352 overlapping square apertures 6 pixels on a side, using astropy's photutils package (Price-Whelan et al. 2018).

The light curve demonstrates the smoothly varying bright-dim-bright pattern, which is visible to the eye in Figure 2. The time from peak to peak is 8 s, yielding a rotation period of roughly 16 s, assuming a simple double-peaked light curve. The amplitude is about one magnitude, implying an axis ratio
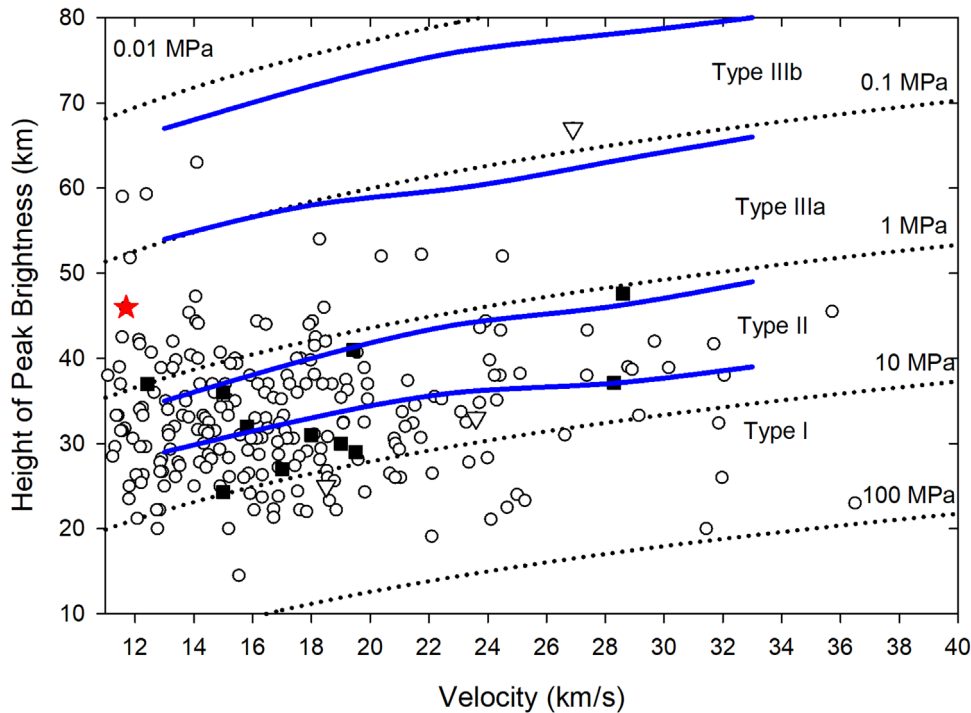
Figure 6. Height at maximum luminosity as a function of entry velocity for meter-sized impactors. The USG 20200918 fireball is shown as a red star. The dotted lines are constant values of dynamic pressure and provide a proxy for strength. Black squares are meter-sized meteorite dropping fireballs, while inverted triangles represent ground-based fireball network observations of meter-sized objects (Brown et al. 2015). Open circles are from the CNEOS-JPL fireball database. See text for description of blue lines associated with various fireball types using model interpretation.

of $\sqrt{2.5} \approx 1.6$. The object was seen at an apparent magnitude that is one to two magnitudes fainter than the predicted value of 11.5. No accompanying streaks indicative of a companion object were seen during visual inspection.

Could the object be a meteor? First, the variation in light curve across the image and abrupt end are not consistent with a meteor trail (Beech & Hargrove 2004). The abrupt end, in particular, would mean the exposure had to stop during the luminous flight, which is highly unlikely given that typical meteor durations at such magnitudes are of order a few tenths of a second (Fleming et al. 1993). Second, if the object were an actual meteor it would have to be much closer (range of order 100 km), and so it would be out of focus (Jenniskens et al. 2004).

To examine whether there is any sign of the trail being out of focus relative to the stars, the cross-sectional profiles of the trail and of nearby stars was extracted as shown in Figure 8. The average profile for the stars is constructed from 1498 stars near the trail and sliced along the same direction as cross sections of the trails. The stars have a FWHM of 2.30 pixels under a 1D Gaussian fit. This is consistent with the ATLAS image's overall stellar FWHM of 2.42 pixels, computed automatically by their software. The profile for the trail is constructed from cross sections taken at the locations of the apertures used to extract the light curve of Figure 7. The trail displays a slight (approximately 1 pixel) curvature from one end to the other, probably due to optical effects. As a result, stacking all 352 cross sections and then fitting a Gaussian profile slightly overestimates the trail's width, coming in at a 2.58 pixels FWHM. To better estimate the true width of the trail, we split it into 20 segments, each consisting of 17 to 18 adjacent cross sections, chosen empirically to provide reasonable time resolution and sufficient signal-to-noise. The mean FWHM of

the trail obtained in this manner is 2.37 ± 0.31 pixels, effectively the same as that of the stars. We conclude that there is no evidence that the trail is close enough to the telescope to undergo defocusing, and hence cannot be a meteor or any in-atmosphere object.

5. Combining the USG and ATLAS Astrometric Data

The USG fireball detection and the ATLAS image streak provide two independent constraints on the location of the object in question. In this section we ask: Are they dynamically consistent with each other? We will see that the answer is yes, solidifying the linkage of these two objects as well as providing some refinement of the USG velocity measurement.

To investigate this question, dynamical simulations of the USG bolide were performed to determine whether or not its motion could bring it to the correct location on the ATLAS image. The simulations used the RADAU (Everhart 1985) integrator to model the object along with the Earth, Moon, Sun, and other planets (as derived from the DE405 ephemeris; Standish 1998) backwards to the time of the ATLAS image.

The Bayesian fitting package MultiNest (Feroz et al. 2011) was used (through its Python interface PyMultiNest; Buchner 2016) to determine what values of the fireball position and velocity components produce a best match to the streak seen on the ATLAS image.

The best fit was determined by minimizing a χ^2 function to four observables, namely, the R.A. and decl. of the end of the streak on the ATLAS image ($304.0814°$ and $+7.1452°$, respectively, each ± 1 pixel $= 1''.86 \approx 5 \times 10^{-4}$ deg), the on-image angle of the streak ($122.25 \pm 0.3°$ clockwise from the lower edge of the image), and the apparent magnitude (12.5 ± 0.2).
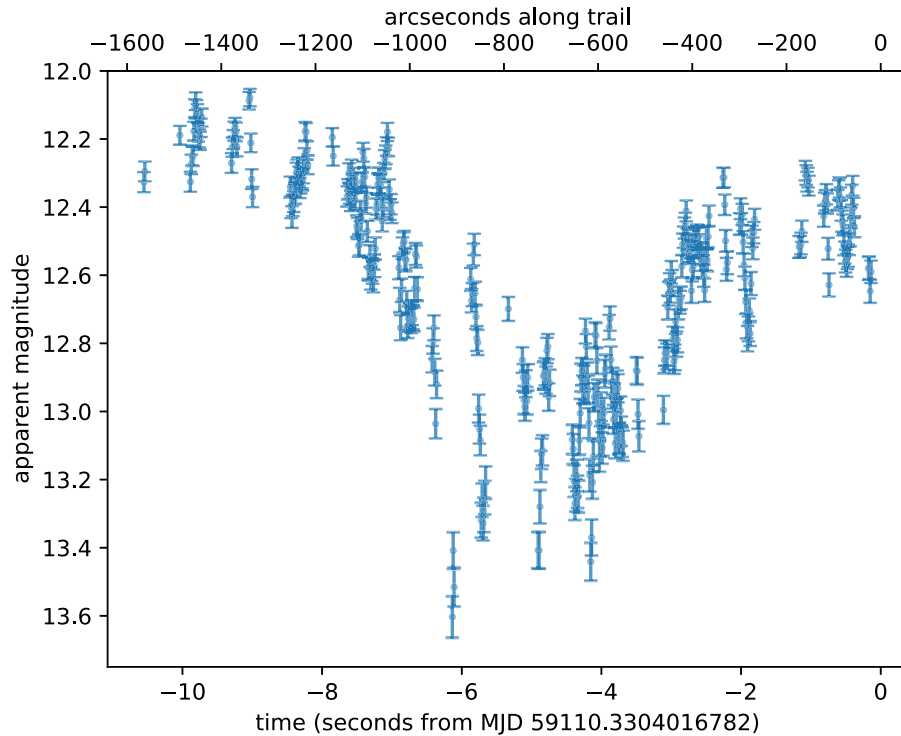
Figure 7. Apparent *c*-band (cyan) magnitude along the ATLAS trail. Time and trail length are measured from shutter closure, assuming the rate of motion calculated in this work. Regions of the trail less than 8 pixels from the center of a star have been masked out.

Seven parameters were fit, six with Gaussian priors centered on the nominal USG position/velocity values listed in Table 1. Since the USG reports do not provide uncertainties, our priors assumed $\pm 1\,\mathrm{km\ s^{-1}}$ for each of the velocity components, $\pm 0.25°$ for the latitude and longitude, and ± 10 km for the altitude of the bolide. The seventh fitted parameter, the absolute magnitude, is not reported, so we adopted a uniform prior for H running from 31 to 34.

The fitting process was repeated 10 times to ensure consistency. There were no statistically significant differences between the fits, so the result of a typical run are presented here. The marginal probability distributions of the fitting are displayed in Figure 9. All the fits are consistent with the USG values, with the exception of a fraction of a degree shift in latitude/longitude and a preference for a slightly higher velocity. The overall best-fit (lowest χ^2) values are shown in Table 1 and will be adopted here as our best estimate of the object's true contact state. This gives a refined velocity vector with a total speed of $12.7\,\mathrm{km\ s^{-1}}$ versus the nominal USG value of $11.7\,\mathrm{km\ s^{-1}}$. The overall parameter fit matches the termination end of the streak within an arcminute, the slope angle to within 0.168 of a degree, and the magnitude to within 0.14 magnitudes. Back-integrating an uncertainty cloud generated from the best-fit values results in the orbit elements listed in Table 5 and the modified orbit shown in Figure 3.

From this result, we can confidently conclude that the USG and ATLAS objects are completely consistent with each other, offset by a small velocity difference that is well within previously reported USG speed uncertainties (Devillepoix et al. 2019). In fact, the best-fit values effectively tell us what the inclusion of the ATLAS image as a constraint does to the orbital solution. By folding that information in, we can see that the object's arrival velocity was actually slightly higher than

that derived by consideration of the USG data alone. This provides additional confidence that the object was not in a geocentric orbit, pushing it clearly to an arrival from heliocentric orbit.

The absolute magnitude of the object is only loosely constrained, but the best-fit value of $H = 32.5$ corresponds to a 0.8, 1.8, and 3.0 m diameter for albedos of 0.25, 0.05, and 0.02, respectively. This makes it one of the smallest asteroids ever observed in space, as will be discussed in the next section.

6. On-image Object Origin

The USG fireball and the ATLAS object could either be the same object or two different ones. Since Occam's razor suggests they are the same object, we will discuss this possibility first, and then return to the less likely case. If the USG and ATLAS detections are the same object, then it is almost certainly natural.

First, the USG entry orbit is not bound to Earth. Though there is man-made material in heliocentric orbit, the bulk of it is in geocentric orbit and the coincidental reentry of a substantial man-made object from heliocentric orbit is extremely unlikely. Moreover, the high inclination of the USG orbit is not consistent with a space-age launch into a heliocentric orbit as it far exceeds typical escape speeds for interplanetary missions.

The impact speed of $11.7\,\mathrm{km\ s^{-1}}$ puts it just above the unbound-from-Earth threshold at $11\,\mathrm{km\ s^{-1}}$. Could measurement uncertainty be masking what was actually a bound orbit? To obtain a rough estimate of the possible velocity error (the USG reports no uncertainties), we note that ATLAS was taking 30 s exposures, and that 30 s earlier or later and the object would have been off the frame. ATLAS images are about $5°$ wide, which at 6000 km corresponds to a distance of $6000\,\mathrm{km}\sin 5° = 500$ km. Assuming the worst case of
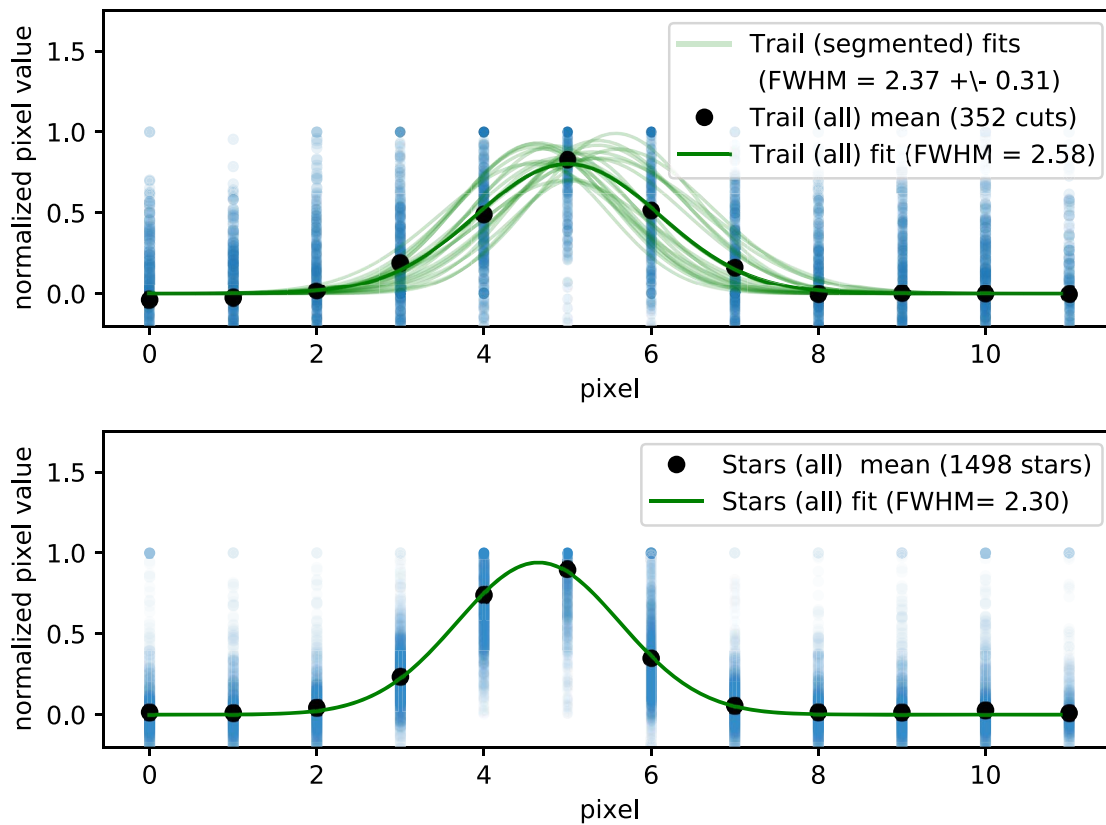
Figure 8. The cross-sectional width of the ATLAS image trail. In the upper panel, the best-fit Gaussian cross section of the entire trail with respect to a hypothetical straight line between the trail's start and end is shown in dark green. This fit has a FWHM of 2.58 pixels. However, the trail has a slight curvature that broadens this distribution. When the trail is broken up into short segments and fit individually (light green lines), these show a smaller FWHM (2.37 ± 0.31), which is consistent with the stars in the image. This result indicates that the trail is not close enough to the telescope to undergo any defocusing. In the lower panel, cross sections of nearby stars, sliced along the same direction used to construct the trail cross sections, are shown for comparison.

tangential motion, a 500 km difference over the less than 10 minute (∼600 s) interval between the ATLAS image and the USG detection requires a velocity error of about 1 km s^{-1}. As such, we cannot strictly exclude a velocity of 10.7 km s^{-1}, that is, on a bound—but only just—orbit from the ATLAS data. Any normal component to the object velocity would mean an even higher speed, further increasing the likeliness of the object having an unbound orbit.

If the object was artificial, it must have been large. The initial estimated mass of 8600 kg derived from the USG energy of 0.14 kt is inconsistent with a small, highly reflective rocket body or satellite. For comparison, the total mass of the Soyuz MS spacecraft is 7080 kg; its descent module, 2950 kg.[8] The unexpected arrival of such a large man-made object is extremely unlikely.

The radiant azimuth of the USG detection at 13° from north would put it on a hypothetical geocentric orbit near 103° inclination to Earth's equator if its speed were low enough to be bound. This is within the range of inclinations typical of Sun-synchronous orbits: 103° corresponds to a Sun-synchronous orbit with a 2 hr period, orbiting at an altitude of 1681 km.[9] However, all such large satellites are cataloged and no predicted reentries occurred near the impact time. Moreover, any satellite decaying from low Earth orbit (LEO) would have a much lower reentry speed, nearer 8 km s^{-1}, and outside our

bounding range. Thus, if the ATLAS and USG detections are the same object, they are very difficult to reconcile with an artificial object.

If the USG and ATLAS detections were separate objects, could the ATLAS telescopic image be a coincidentally located artificial object? If that were the case, the USG velocity must have been off by >1 km s^{-1} (for the meteoroid to be off the ATLAS frame), and a different object traveling (i) in the right direction at (ii) the right brightness at (iii) the right time and at least approximately (iv) at the right speed must have been in frame. Fortunately, all objects >10 cm are known, tracked, and cataloged in LEO (National Research Council 2011) with catalogs publicly available at Space-Track.org.[10]

The speed is less well constrained because the trail starts (or ends) outside the image. But the object in the ATLAS image must travel at least 1579″ (the length of the trail on-image) in 30 s, or at least 53″ per second. An object in LEO (which might be traveling 200″ s^{-1} or more) could make a comparable streak length, and at an apparent magnitude of 11.4, a satellite at 3000 km would be of order 1 m^2 cross-sectional area. The inclination is reasonable for a man-made object, as well: if we assume the motion seen in the image is a circular orbit in LEO, then its orbital inclination is roughly the angle of the trail with the x-axis, that is, 58° (or 180° − 58° = 122°, depending on which direction it is moving). The former value is near the heavily populated region of LEO containing nonpolar inclined orbits
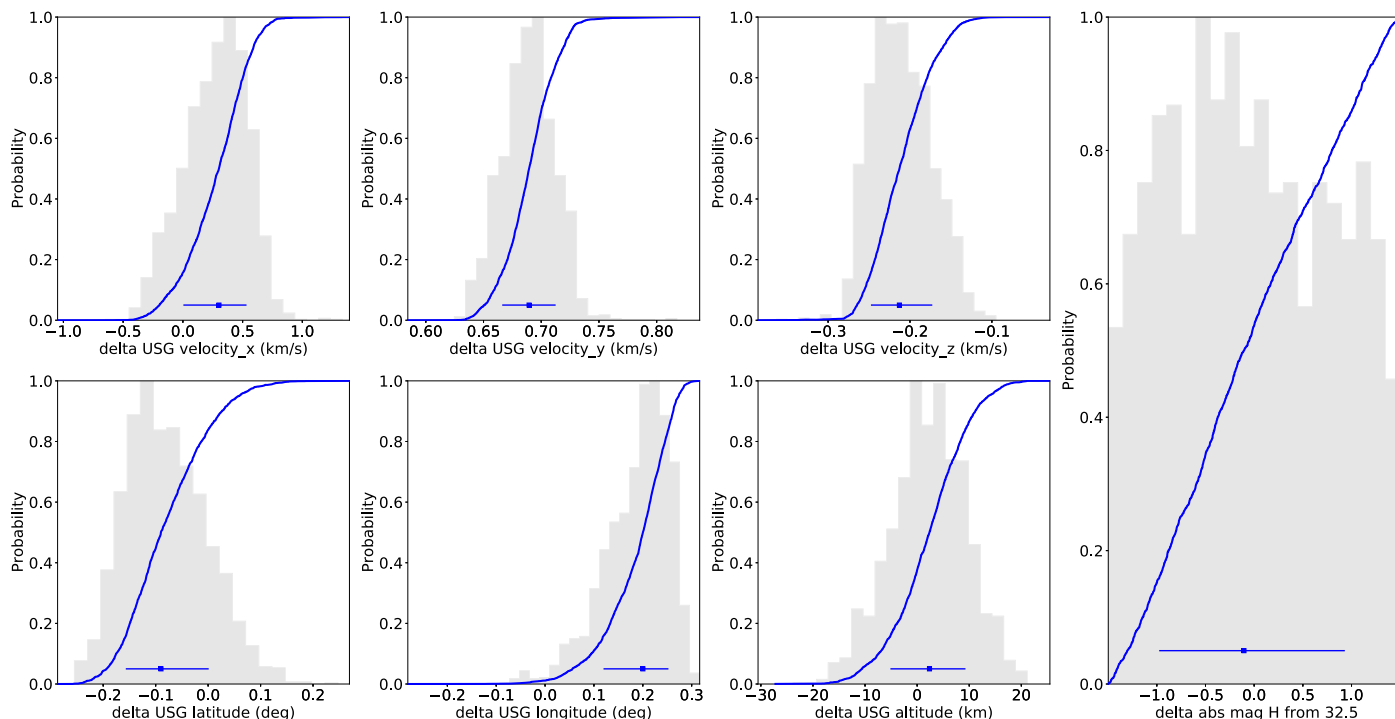
Figure 9. Marginal probability distributions (in gray) from one of the parameter fitting runs. The blue points with horizontal uncertainty bars show the median values with their 1σ uncertainties. The fitted parameters are displayed as differences from the nominal USG values and from a nominal absolute magnitude H of 32.5. The blue curves show the cumulative probability distributions.

(peaking near 53°; see Figure 11), so there are certainly satellites in this region.

Fortunately, the geometry allows us to exclude objects in LEO because they would be in the Earth's shadow. The Sun had set at the ATLAS site at the time in question, and sunlight was still illuminating objects only at altitudes greater than 3400 km above sea level. So all of LEO would have been in shadow while the meteoroid—at an altitude of 6000 km—would have been in full sunlight at the same time. Figure 10 illustrates the geometry during the ATLAS observation. If the object were a satellite, it would have to be in the much more sparsely populated region above 3400 km. Though the possibility of an artificial object cannot be positively excluded to this point in our analysis, we can conclude that the ATLAS and USG detections have a very high probability of being the same natural object.

To fully eliminate the possibility of the ATLAS detection being that of a man-made object, we downloaded the full catalog of element sets for all tracked orbiting objects from Space-Track.org.[11] We use the TLE (three-line element) formatted file,[12] although we have used the older NORAD TLE (two-line element) terminology to refer to the cataloged objects. The 21,944 cataloged TLEs were used to plot the object trajectories with respect to the ATLAS image. Three objects were found to intersect the image (see Figures 1 and 11): object 44525 passed though the field of view, while object 21253's and object 26583's paths begin in the image and terminate outside. As can be seen in Figure 11, object 44525 and object 21253 are in LEO and therefore in the Earth's shadow. They could not be (and are not) visible in the image.

Object 26583 is well outside the Earth's shadow and is visible in the ATLAS image at the correct location, distinctly different from the candidate image streak.

This exercise highlights the challenge of discriminating a telescopic preimpact detection of a meter-sized fireball—most of which have coarse state-vector accuracy from in-atmosphere measurements—from satellites. The proliferation of LEO satellites will make future associations harder.

Another consideration is the possibility of the image streak being that of an in-atmosphere natural or man-made object such as a meteor, reentry debris, or airplane. Section 4 describes a detailed analysis of the light curve of the ATLAS detection. There is no evidence of defocusing expected for such a near-field object, so that possibility can be discounted.

Having argued the image streak is not due to an artificial or in-atmosphere object, we now address the possibility that the image streak was caused by another natural out-of-atmosphere object distinct from that reported by USG. To do this, we will compute the number of objects expected to appear in the image at the correct magnitude and on-sky speed, and show that is it very low, making the coincidental appearance of another object very unlikely.

Brown et al. (2002) provides a power law relating the diameter of an impacting object with the cumulative number of objects of that diameter or greater impacting the Earth in a year. The number of impacts can be directly mapped to a near-Earth number density of these objects by using a cylindrical volume of space determined from the cross-sectional area of the Earth and the average speed of impactors (we use 20 km s^{-1}). The sizes of objects to be considered are bound by two factors: the closest possible distance of the object based on the the object being outside the Earth's shadow, and the furthest possible distance of a solar system object that could result in a streak as long as that observed on the image. Using standard
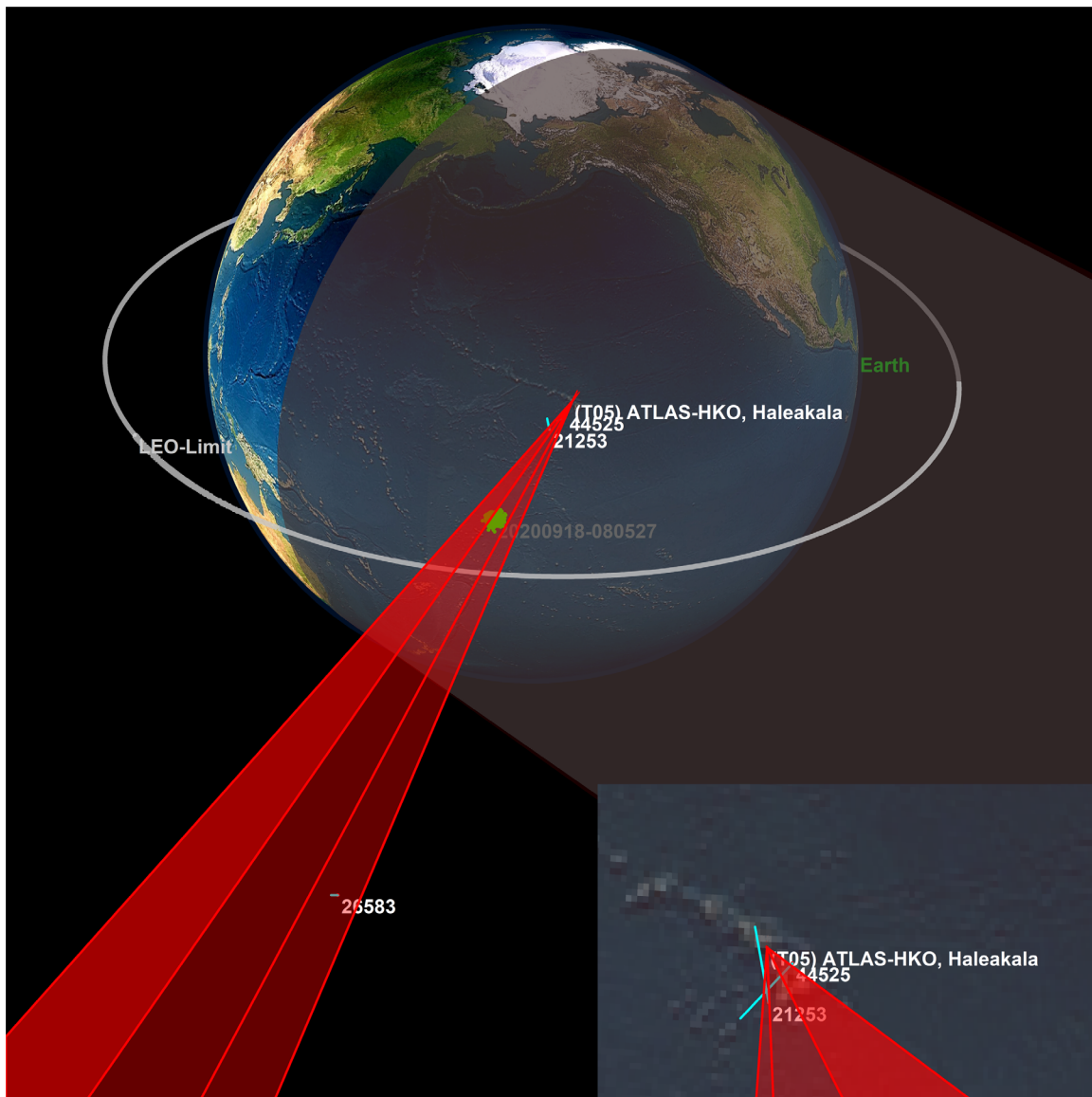

Figure 10. An illustration of the Earth's shadow's alignment at the time of image capture. The umbral shadow is shown in dark gray. The penumbral shadow is imperceptibly larger than the umbral at such close proximity to the Earth. The gray circle is the upper "limit" of LEO orbits at $H_{\text{LEO}} = 2000$ km. The red wedge is the volume of space covered by the image. The irregular green area is the predicted uncertainty of the object. The numbered blue lines in both the main image and inset represent the motions of all tracked artificial objects in the field of view of the image, with their NORAD TLE numbers. Within the field of the image, any object inside the LEO limit, and substantially further, is in the Earth's shadow and would not be visible in the image. Only three tracked objects are within the image field, and only one of them (26583) is outside the Earth's shadow and is visible. This object is evident in the ATLAS image reproduced in Figure 2.

relationships of absolute and visual magnitude, together with the object's phase angle, and relationships of asteroid diameter and absolute magnitude, we can estimate the diameter of both nearest and furthest possible objects that could result in the brightest ($m = 12.1$) visual magnitude captured (Figure 7). For these calculations, we assume representative object albedos and slope parameters of 0.15.

Extending the line of sight of the object streak outside the Earth's shadow results in a nearest object distance of approximately 3000 km with an object diameter of 0.73 m. Assuming the worst case of an object moving at the geocentric solar escape velocity of 72 km s^{-1}, the furthest an object could be from Earth to produce the on-image streak subtending $0.442°$ (Table 6) would be approximately 280,000 km with an object diameter of 71 m. A high estimate of the total number of observable $m = 12.1$ objects at any point in time is arrived at by summing the numbers of objects at incremental distances and magnitudes between the two limits, and dividing by the portion of the sky covered by the ATLAS image ($5.5° \times 5.5°/ 41,000°^2$). At the near limit, we arrive at 8×10^{-8} objects expected on the image and 3×10^{-7} at the furthest limit. These numbers slowly increase with distance and required size, with the volume to distance of exponent of 3 being strongly offset by the 2.7 index of the Brown et al. (2002) power law and the $\log_{10}$ relationship of magnitude and distance. Summing across regular intervals of distance, we arrive at an approximate number of $m = 12.1$ or larger objects on any such ATLAS image of 3.5×10^{-6} objects. This strongly suggests that the image streak is the same object as detected in the USG fireball observation and not an unassociated natural object.
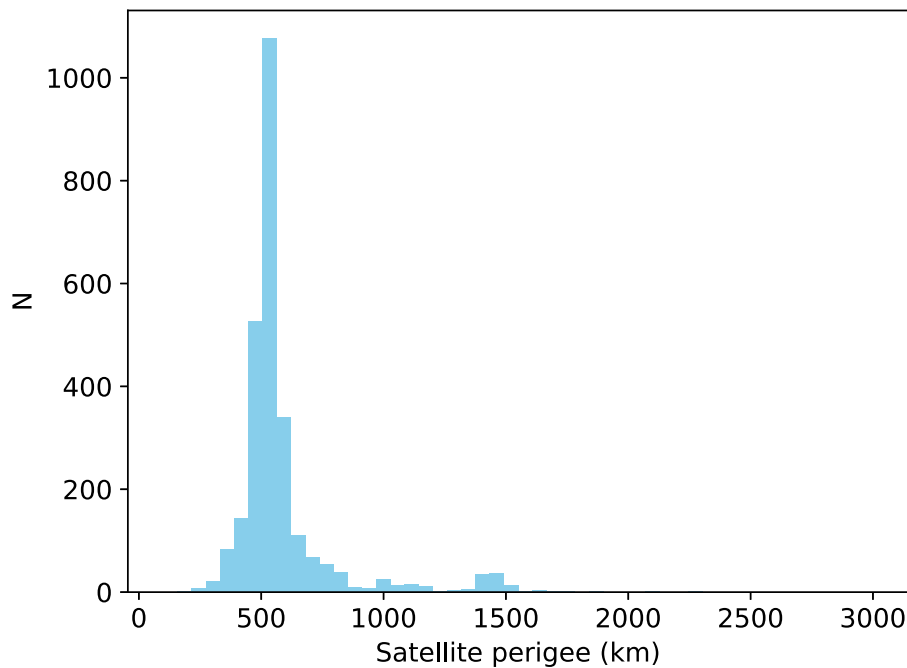
Figure 11. A histogram of Earth satellite perigee values, from the Union of Concerned Scientists Database (retrieved 2021 May 13).

Table 6
Object Streak

	Predicted	On-image	Difference
North-northeast end-point R.A. (deg)	300.807	304.319[a]	
North-northeast end-point decl. (deg)	7.359	7.516[a]	
South-southwest end-point R.A. (deg)	300.168	304.080	3.912
South-southwest end-point decl. (deg)	6.276	7.142	0.866
Angular difference at south-southwest point (deg)			3.981
Streak ΔR.A. (deg)	−0.369	−0.239[a]	0.130[a]
Streak Δdecl. (deg)	−1.083	−0.373[a]	0.710[a]
Streak length (deg)	1.255	0.442[a]	−0.813[a]
Slope counterclockwise from west (deg)	120.546	122.647	2.101

Notes. Comparison of predicted nominal object streak based on USG observation and observed north-northeast truncated streak on the actual image.
[a] Value impacted by edge truncation.

7. Subsequent Image Search

Subsequent to work performed to determine an object trajectory which best fit both the on-image streak and the USG observations (see Section 5), new image searches were performed based on this new trajectory. These searches suggested two additional surveys may potentially have captured the object.

The first is an image quartet taken by the Catalina Sky Survey using the Mount Lemmon telescope.[13] The images G96_20200918_2B_N27128_01_0001, _0002, _0003, and _0004 were taken 2.5 to 2.0 hr prior to contact where the object would have been at an approximate visual magnitude of 18. Using 20,000 clones generated in the best-fit process, we calculate a 10% probability of the object being on the first image of the quartet, increasing to 20% on the fourth image. We estimate a trailing loss of 4.5–5 mag, resulting in an effective visual magnitude of 22.5–23. With Mount Lemmon's limiting magnitude of 21.5, the object would likely not be visible in the images. Visual blinking of the image quartet using an automated blink and pan using the DS9 software (Joye & Mandel 2003) did not yield any detection of a moving object. Our software permits us to highlight the locations of known objects in DS9. Objects significantly brighter were visible in the images, but objects of similar magnitude to our target meteoroid were not, consistent with the nondetection. We also performed a visual scan of median-subtracted images; again, no object was found. Finally, we performed a shift and stack process shifting the images by aligning the projected position of the object on each image and stacking the results. Stacking four images yields only a $\sqrt{4}/2.5 < 1$ mag increase in sensitivity. Adjusting Mount Lemmon's limiting magnitude of 21.5 to 22.5 due to stacking places the object at the limit of visibility. Again, no object was detected in either the stacked original images or stacked median-subtracted images.

Second, a recent implementation of a Zwicky Transient Facility (ZTF)[14] image catalog[15] import into our image database yielded an additional potential image capture. ZTF image ID 135630722, taken 43 minutes before impact, has an approximately 80% probability of containing the object. If visible, the object would appear as a $10'$ ($566''$) streak. However, the object's visual magnitude of approximately 16.0 at this time combined with a trailing loss of nearly 7 magnitudes render the object much dimmer than ZTF's limiting magnitude of 20.5. Still, a visual scan was performed but no object was found.

FROSTI image searches were performed against an ever increasing set of current and historical image catalogs in an attempt to locate additional possible imagery: ATLAS Haleakalā and Mauna Loa (and recently Altas Sutherland Observing Station and El Sauce), the Canada–France–Hawaii

---

[13] https://catalina.lpl.arizona.edu/about/facilities

[14] https://www.ztf.caltech.edu/
[15] https://irsa.ipac.caltech.edu/frontpage/

Telescope (CFHT), Catalina (Mount Lemmon, Mount Bigelow, Catalina Follow-up, Kuiper, Bok, and Siding Springs), CNEOST, DeCAM, the Hubble Space Telescope, LONEOS, Pan-STARRS 1 and 2, the Wide-field Infrared Survey Explorer (WISE) and NEOWiSE, the ZTF, and all contributing observatories to the Minor Planet Centre Sky Coverage Pointing Data.[16] No additional possible preimpact images were found.

8. Discussion

The rotation period inferred for the object studied here is short but not unprecedented. Hatch & Wiegert (2015) examined the published data for the 88 smallest known NEAs (all with diameters less than 60 m) and found that the average rotation period of the sample is 40 minutes, with smaller asteroids rotating faster. Three asteroids in their sample were found to have rotation periods (retrieved from the Asteroid Light Curve Photometry Database, ALCDEF;[17] Warner et al. 2009) below 60 s: 2010 WA (a 3 m diameter S type) with a period of 31 s; 2010 JL88 (a 13 m diameter S type) with a period of 25 s; and 2014 RC (a 13 m diameter S type) with a rotation period of 15.8 s. The first two of these asteroids have a quality rating in ALCDEF of $U = 3$, which is the highest rating, while the third has no rating. We conclude that the rotation period of 16 s inferred here is in line with those of other known small asteroids.

Hatch & Wiegert (2015) also collected data on the 92 smallest NEAs with known axis ratios; this sample includes diameters up to 300 m. They found that the mean and median axis ratios are 1.43 and 1.29, respectively, though axis ratios above 2 were not uncommon. We conclude that the axis ratio of 1.6 for this event as determined from the ATLAS light curve (Figure 7) is consistent with those of other small NEAs.

Assuming a rotation period of 16 s and a diameter of 3 m, we can also work out the minimum binding strength of the meteoroid. Using the formula for the limiting tensile strength at the center of a rotating sphere able to just provide sufficient centripetal acceleration to keep the sphere intact from Kadish et al. (2005) for a 3 m diameter sphere with bulk density of 1600 kg m^{-3}, we find a limiting strength of <1 kPa. This is well below the earliest fragmentation pressure and therefore physically plausible.

The 3 m diameter determination from Section 3 and the best-fit absolute magnitude $H = 32.5$ from Section 5 necessitate a very low albedo of 0.02 under the standard assumptions of asteroid photometry. Is this reasonable? Only 10% of NEAs observed by the NEOWISE have an albedo less then 0.03%, 5% less than 0.02 (Wright et al. 2016). However, fully 25% of NEOWISE-observed NEAs belong to an albedo population peaking at an albedo of 0.03. Factors which could lead to higher visual magnitudes and therefore higher absolute magnitudes and lower albedo estimates include shape profiles and self-shadowing. Assuming an oblate spheroid, the above estimated 1.6 axis ratio could easily result in a smaller face of the object reflecting sunlight to the observer than would be assumed for a spherical object. This is, of course, an argument of possibility, in that an object could equally have a larger face reflecting. If the object is more irregular in shape, as would be reasonable for a low-mass rubble pile, then self-shadowing would begin to take effect, lowering the overall brightness of the object for an equivalent albedo. Self-shadowing is more influential at higher phase angles. With the USG object at a phase angle at nearly 56° self-shadowing could very well be a factor in the larger magnitude estimation.

Given that the object arrived on the orbit listed in Table 5, we might ask about its likely escape region from the main belt. The orbit is certainly consistent with an evolved asteroidal orbit rather than a cometary one. The NEO model of Granvik et al. (2018) provides source region probabilities as a function of a, e, i, and absolute magnitude H. The H of our object, at about 33, is well below the range of $17 < H < 25$ considered by Granvik et al. (2018), but if we examine the source region probabilities of their smallest model bin (central $H = 24.785$) we find the probability is 70% for the main belt ν_6 resonance, 19% from the Hungarias, and 11% from the 3:1 and other source regions negligible.

The low albedo and structural weakness of the object would be consistent with a C-complex NEA. Given the high probability of escape from the ν_6 resonance, it is interesting to note that Marsset et al. (2022) have found that the debiased fraction of C/D/P NEAs is almost 40% of the total with present orbits associated with that source region. They also report a higher abundance of D-type NEOs than previously found from all escape regions, including the ν_6. In this context, that the USG 20200918 fireball appears consistent with a C-complex meteoroid is not surprising.

Though the USG object was telescopically detected when unusually close and small, the event does refuse superlative labeling, though barely. At the time of impact, the object was only the fifth Earth-impacting object to be detected in space. Subsequent to 2020 September 18, two additional impacting objects, 2022 EB5[18] and 2022 WJ1,[19] were observed in space prior to impact on 2022 March 11 and 2022 November 19, respectively. At the time of the USG event, the ATLAS observation was the closest observation of a natural preatmospheric object. This proximity analysis was performed using the Python astroquery.mpc[20] package to download all observation times of the six Earth-impacting object observations as well as the 47 near-Earth fly-bys whose minimal geocentric distance was less than that of the USG object (see Table 7). Then, using the JPL Horizons Telnet ephemeris system,[21] we acquired the nominal geocentric distance for each object observation. Two objects having a telescopic observation distance of less than the USG object's 11,920 km geocentric distance are 2022 EB5, at a calculated 11,854 km, and 2023 CX1, at 11,125 km. Prior to 2020 September 18, the closest object observation was that of 2018 LA, at approximately 22,000 km. A superlative that does hold for the ATLAS image of the USG event is that it is the closest initial observation of a preatmospheric object, far exceeding 2022 EB5, at 115,000 km, and 2021 UA1, at 147,000 km.

By no means is the USG object the smallest object observed in space. The MPCORB,[22] NEODyS,[23,24] and JPL-SSD Small Body[25] asteroid and NEA databases all list 2008 TS26 at an

---

[16] https://www.minorplanetcenter.net/iau/info/PointingData.html

[17] www.alcdef.org

[18] http://www.cbat.eps.harvard.edu/iau/cbet/005100/CBET005108.txt

[19] https://www.jpl.nasa.gov/news/nasa-program-predicted-impact-of-small-asteroid-over-ontario-canada

[20] https://astroquery.readthedocs.io/en/latest/mpc/mpc.html#

[21] Telnet: horizons.jpl.nasa.gov 6775.

[22] https://www.minorplanetcenter.net/iau/MPCORB/MPCORB.DAT

[23] https://newton.spacedys.com/~neodys2/neodys.cat

[24] https://newton.spacedys.com/~neodys2/neodys.ctc

[25] https://ssd.jpl.nasa.gov/dat/ELEMENTS.UNNUM

Table 7
Nearest Preatmospheric Observations of Natural Objects

Object	d_{min}(au)	Initial Observation		Last Observation		Closest Observation	
		Date/Time	10^3 km	Date/Time	10^3 km	Date/Time	10^3km
Earth Impactors							
2008 TC3		2008 Oct 6.277 67	493	2008 Oct 7.073 10	34	2008 Oct 7.073 10	34
2014 AA		2014 Jan 1.262 57	417	2014 Jan 1.310 81	396	2014 Jan 1.310 81	396
2018 LA		2018 Jun 2.343 295 16	390	2018 Jun 2.500 959 16	220	2018 Jun 2.500 959 16	220
2019 MO		2019 Jun 22.329 285 15	576	2019 Jun 22.424 624 15	480	2019 Jun 22.424 624 15	480
2022 EB5		2022 Mar 11.808 476 10	115	2022 Mar 11.886 840 10	12	2022 Mar 11.886 840 10	12
2022 WJ1		2022 Nov 19.203 482 01	128	2022 Nov 19.327 456 02	27	2022 Nov 19.327 456 02	27
2023 CX1		2023 Feb 12.845 917 07	233	2023 Feb 13.119 527 07	11	2023 Feb 13.119 527 07	11
Fly-bys							
2008 EK68	0.0000000	2008 Mar 5.440 60	1622	2008 Mar 5.480 66	1650	2008 Mar 5.440 60	1622
2011 AE3	0.0000000	2011 Jan 4.238 29	936	2011 Jan 4.281 06	946	2011 Jan 4.238 29	936
2016 QY84	0.0000000	2016 Aug 29.283 86	2206	2016 Aug 29.408 78	2241	2016 Aug 29.283 86	2206
2011 CH22	0.0000000	2011 Feb 7.526 27	1737	2011 Feb 7.544 97	1743	2011 Feb 7.526 27	1737
2017 UL52	0.0000000	2017 Oct 21.300 85	1627	2017 Oct 21.474 99	1659	2017 Oct 21.300 85	1627
2010 XC	0.0000000	2010 Dec 1.306 59	2731	2010 Dec 1.364 95	2710	2010 Dec 1.364 95	2710
2012 HA34	0.0000000	2012 Apr 30.379 29	2402	2012 Apr 30.981 38	1875	2012 Apr 30.981 38	1875
2009 JE1	0.0000000	2009 May 4.365 74	4118	2009 May 4.434 11	4079	2009 May 4.434 11	4079
2008 JD33	0.0000000	2008 May 15.286 89	5061	2008 May 15.398 72	5088	2008 May 15.286 89	5061
2010 SV15	0.0000000	2010 Sep 30.278 50	8429	2010 Sep 30.378 66	8492	2010 Sep 30.278 50	8429
2012 TC4	0.0000001	2012 Oct 4.467 661 23	4420	2017 Dec 14.300 667 10	30353	2017 Oct 12.161 214 19	65
2017 VL2	0.0000008	2017 Nov 10.475 21	787	2017 Nov 26.345 80	12206	2017 Nov 10.475 21	787
2021 VD8	0.0000010	2021 Nov 10.277 723 02	719	2021 Nov 12.556 600 03	3022	2021 Nov 10.277 723 02	719
2022 GX2	0.0000018	2022 Apr 2.316 494 11	2350	2022 Apr 3.178 171 11	3062	2022 Apr 2.316 494 11	2350
2021 XK1	0.0000034	2021 Dec 2.342 781 05	4959	2022 Jan 9.357 330 04	36101	2021 Dec 2.342 781 05	4959
2021 AY5	0.0000100	2021 Jan 12.503 875 10	9245	2021 Feb 18.285 49	23557	2021 Jan 12.503 875 10	9245
2020 AP1	0.0000100	2020 Jan 4.371 33	879	2020 Jan 5.441 63	1359	2020 Jan 4.371 33	879
2014 WE6	0.0000100	2014 Nov 17.194 35	1358	2014 Nov 21.466 686 02	3001	2014 Nov 17.194 35	1358
2007 XO	0.0000100	2007 Dec 4.271 09	7549	2007 Dec 4.452 58	7242	2007 Dec 4.452 58	7242
2002 EM7	0.0000100	2002 Mar 12.306 75	3805	2002 Apr 6.268 06	27112	2002 Mar 12.306 75	3805
2004 FU162	0.0000200	2004 Mar 31.277 44	357	2004 Mar 31.307 99	329	2004 Mar 31.307 99	329
2022 BN2	0.0000200	2022 Jan 27.382 231 10	1271	2022 Jan 28.421 569 11	508	2022 Jan 28.421 569 11	508
2016 AH164	0.0000200	2016 Jan 13.312 27	696	2016 Jan 18.286 488 08	3592	2016 Jan 13.312 27	696
2014 HB177	0.0000200	2014 Apr 29.360 76	3782	2014 May 5.034 69	850	2014 May 5.034 69	850
2020 SP6	0.0000200	2020 Sep 28.201 621 22	2168	2020 Nov 18.278 968 03	43572	2020 Sep 28.201 621 22	2168
2015 KE	0.0000300	2015 May 18.209 95	4004	2016 Aug 25.248 26	6646	2015 May 18.209 95	4004
2018 WG2	0.0000300	2018 Nov 29.239 15	904	2018 Nov 30.732 895 22	203	2018 Nov 30.732 895 22	203
2021 XA6	0.0000300	2021 Dec 12.251 668 22	537	2022 Jan 2.873 97	10521	2021 Dec 12.251 668 22	537
2018 VP1	0.0000400	2018 Nov 3.272 495 02	451	2018 Nov 16.240 265 03	11303	2018 Nov 3.272 495 02	451
2020 HC11	0.0000400	2020 Apr 17.364 573 14	62789	2020 Sep 17.592 464 03	72547	2020 May 29.178 15	29435
2018 XQ2	0.0000400	2018 Dec 10.242 30	3675	2019 Jan 7.067 641 01	9841	2018 Dec 10.242 30	3675
2020 VT4	0.0000500	2020 Nov 14.320 628 02	428	2020 Nov 19.266 49	3814	2020 Nov 14.320 628 02	428
2018 DN4	0.0000500	2018 Feb 26.249 92	2524	2018 Feb 26.394 47	2748	2018 Feb 26.249 92	2524
2017 UR2	0.0000500	2017 Oct 19.395 18	1620	2017 Oct 21.266 32	3343	2017 Oct 19.395 18	1620
2017 TU1	0.0000500	2017 Oct 1.411 397 02	11127	2017 Oct 14.105 75	2074	2017 Oct 14.103 13	2074
2011 GP28	0.0000500	2011 Apr 4.364 51	3089	2011 Apr 5.338 46	1864	2011 Apr 5.338 46	1864
2020 QG	0.0000600	2020 Aug 16.432 732 00	198	2020 Aug 18.005 870 00	1317	2020 Aug 16.432 732 00	198
2021 UA1	0.0000600	2021 Oct 25.255 448 01	147	2021 Oct 26.116 061 01	1110	2021 Oct 25.255 448 01	147
2014 LY21	0.0000600	2014 Jun 2.416 12	1345	2014 Jun 2.461 18	1300	2014 Jun 2.461 18	1300
2017 LD	0.0000600	2017 May 16.298 488 13	8555	2017 Jun 30.356 014 01	9991	2017 Jun 5.403 31	1151
2010 VP139	0.0000600	2010 Nov 14.279 11	1688	2010 Nov 14.324 99	1723	2010 Nov 14.279 11	1688
2009 VZ39	0.0000600	2009 Nov 10.272 04	1674	2009 Nov 10.315 46	1646	2009 Nov 10.315 46	1646
2020 GB1	0.0000600	2020 Apr 2.534 924 14	3205	2020 Apr 6.969 728 07	413	2020 Apr 6.969 728 07	413
2020 RD4	0.0000700	2020 Sep 12.498 281 00	2017	2020 Sep 14.241 588 23	538	2020 Sep 14.241 588 23	538
2022 KZ	0.0000700	2022 May 21.450 54	4504	2022 May 25.454 005 20	978	2022 May 25.454 005 20	978
2022 EQ	0.0000700	2022 Mar 2.327 760 10	852	2022 Mar 2.981 452 08	250	2022 Mar 2.981 452 08	250
2023 BU	0.0000700	2023 Jan 21.342 991 09	1376	2023 Jan 31.912 811 15	1197	2023 Jan 26.960 521 07	31

Note. The seven telescopically detected Earth impactors and 47 Earth fly-bys with minimal geocentric distances less than 0.00008 au as provided by NEO Earth Close Approaches web site (https://cneos.jpl.nasa.gov/ca/) with observation times provided by the astroquery.mpc (https://astroquery.readthedocs.io/en/latest/mpc/mpc.html#) Python package. The epoch and geocentric distance in kilometers for the initial observation, the last observation, and the closest observation are arrived at by interpolating ephemerides for the provided objects acquired from the JPL Horizons Telnet ephemeris service (telnet: horizons.jpl.nasa.gov 6775).

absolute magnitude 33.1–33.2 and 2021 BO at 32.9. They both exceed the estimated $H = 32.5$ of the USG event, even without regard to the disproportionately high H due to an exceedingly low albedo.

From the point of view of the FROSTI project and the hope to identify preatmospheric images of objects having produced fireballs, the more than $4°$ discrepancy in object location on the image plane is a matter of concern. We were indeed fortunate that the predicted location of the object and the actual observation of the object were both on the same image, aided by the wide $5.5°$ field of ATLAS. Our underestimate of the real uncertainties of USG events could result in images with fireballs going unflagged by FROSTI, particularly for sky-survey images with small fields. In like scenarios to this event, using standard deviations equal to the USG most significant reported digit appears to underestimate uncertainties. However, a wholesale increase of uncertainty cloud size for all USG events within FROSTI will also generate many false-positive results; granted that the 2020 September 18 detection was somewhat unique given the proximity of the object, thus minimizing the extent of in-sky positional uncertainty. However, experience with visualizing uncertainty cloud behavior as one moves backward in time prior to an impact shows that the decreasing angular size of the cloud due to increased distance and the divergence due to increasing clone spread tend to cancel each other out. Although CNEOS provides data on bolides that would go otherwise optically unobserved, this case study further supports the general result found by Devillepoix et al. (2019), namely, that the USG-derived trajectories are much less precise than those derived from ground-based fireball observations.

9. Summary

The USG 20200918 fireball was the first successful identification from archival imagery of a serendipitous preatmospheric image of an observed fireball. We have shown that the ATLAS detection of a streak just 10 minutes prior to impact is broadly consistent with the CNEOS-listed USG state vector within its large expected uncertainties (Devillepoix et al. 2019), while ruling out confusion from known satellites or an unassociated natural object. Given the large USG uncertainties, the detection via the FROSTI survey was very fortuituous: imaging so near to impact, the large uncertainty was still smaller than the wide ATLAS field of view.

Our analysis of the fireball produces a preferred estimate of 0.4 kt TNT total energy. This is based on a synthesis of the CNEOS and GLM light-curve and infrasound source energies. This energy, together with a preatmosphere speed of 12.7 km s^{-1} measured by combining the USG state vector, suggest a mass of order 23 t. Through comparison with 2008 TC3, which entered at a similar speed and behaved similarly in atmosphere based on the recorded fireball light curve, we suggest the most likely bulk density is also around 1600 kg m^{-3} and associated diameter 3 m. The telescopic light-curve amplitude suggests an axis ratio of 1.6, while the light-curve periodicity is consistent with a rotation period of about 16 s.

The resulting best-fit orbit results in a high probability of escape from the ν_6 secular resonance. The apparent magnitude and size are most consistent with a very-low-albedo, C-complex object. Whether the apparent structural weakness is due to a rubble-pile structure or microporosity is unclear.

The event has demonstrated that the the FROSTI project can add to the collection of in-space imaged Earth impactors, collection of which was previously dependent on precontact object detection. The ATLAS image is the closest ever initial observation of a preatmospheric object, and rivals the observations of 2022 EB5 and 2023 CX1 as one of the closest observations of any such object.

Taken on its own, the absence of reported uncertainties for the USG-calculated object trajectory makes its interpretation more difficult, but was sufficiently accurate in this case to allow us to identify a historical ATLAS image of the object.

ORCID iDs

David L. Clark ⓘ https://orcid.org/0000-0002-1203-764X
Paul A. Wiegert ⓘ https://orcid.org/0000-0002-1914-5352
Peter G. Brown ⓘ https://orcid.org/0000-0001-6130-7039
Denis Vida ⓘ https://orcid.org/0000-0003-4166-8704
Aren Heinze ⓘ https://orcid.org/0000-0003-3313-4921
Larry Denneau ⓘ https://orcid.org/0000-0002-7034-148X

References

Beech, M., & Hargrove, M. 2004, EM&P, 95, 389
Borovička, J., Bettonvil, F., Baumgarten, G., et al. 2021, M&PS, 56, 425
Borovička, J., & Charvát, Z. 2009, A&A, 507, 1015
Borovička, J., Spurný, P., & Brown, P. 2015, in Asteroids IV, ed. P. Michel, F. E. DeMeo, & W. F. Bottke (4th ed.; Tucson, AZ: Univ. Arizona Press), 257
Borovička, J., Spurný, P., & Shrbený, L. 2020, AJ, 160, 42
Borovička, J., Tóth, J., Igaz, A., et al. 2013, M&PS, 48, 1757
Bowell, E., Hapke, B., Domingue, D., et al. 1989, in Asteroids II, ed. R. P. Binzel, T. Gehrels, & M. S. Matthews (Tucson, AZ: Univ. Arizona Press), 524
Brown, P., Spalding, R. E., ReVelle, D. O., Tagliaferri, E., & Worden, S. P. 2002, Natur, 420, 294
Brown, P. G., Wiegert, P., Clark, D., & Tagliaferri, E. 2015, Icar, 266, 96
Buchner, J. 2016, PyMultiNest: Python interface for MultiNest, Astrophysics Source Code Library, ascl:1606.005
Cansi, Y. 1995, GeoRL, 22, 1021

Ceplecha, Z., Borovička, J., Elford, W. G., et al. 1998, SSRv, 84, 327

Ceplecha, Z., & McCrosky, R. 1976, JGR, 81, 6257

Clark, D. L. 2014, PASP, 126, 70

Clark, D. L. 2010, MS thesis, Univ. Western Ontario, https://physics.uwo.ca/~dclark56/frosti/ThesisDavidLClarkFinalv2.pdf

Devillepoix, H. A. R., Bland, P. A., Sansom, E. K., et al. 2019, MNRAS, 483, 5166

Edwards, W., Brown, P. G., & ReVelle, D. 2006, JASTP, 68, 1136

Ens, T., Brown, P. G., Edwards, W., & Silber, E. 2012, JASTP, 80, 208

Everhart, E. 1985, in IAU Colloq. 83, Dynamics of Comets: Their Origin and Evolution, Astrophysics and Space Science Library, Vol. 115, ed. A. Carusi & G. B. Valsecchi (Dordrecht: Reidel), 185

Feroz, F., Hobson, M. P., & Bridges, M. 2011, MultiNest: Efficient and Robust Bayesian Inference, Astrophysics Source Code Library, ascl:1109.006

Fleming, D., Hawkes, R., & Jones, J. 1993, in Meteoroids and Their Parent Bodies, ed. J. Stohl & I. Williams (Bratislava: Astronomical Inst. of the Slovak Academy of Sciences), 261

Granvik, M., Morbidelli, A., Jedicke, R., et al. 2018, Icar, 312, 181

Hatch, P., & Wiegert, P. A. 2015, P&SS, 111, 100

Heinze, A. N., Tonry, J. L., Denneau, L., et al. 2018, AJ, 156, 241

Jenniskens, P., Albers, J., Tillier, C. E., et al. 2018, M&PS, 53, 2445

Jenniskens, P., Fries, M., Yin, Q.-Z., et al. 2012, Sci, 338, 1583

Jenniskens, P., Gabadirwe, M., Yin, Q., et al. 2021, M&PS, 56, 844

Jenniskens, P., Jehin, E., Cabanac, R. A., Laux, C. O., & Boyd, I. D. 2004, M&PS, 39, 609

Jenniskens, P., Shaddad, M. H., Numan, D., et al. 2009, Natur, 458, 485

Joye, W. A., & Mandel, E. 2003, in ASP Conf. Ser. 295, Astronomical Data Analysis Software and Systems XII, ed. H. E. Payne, R. I. Jedrzejewski, & R. N. Hook (San Francisco, CA: ASP), 489

Kadish, J., Barber, J. R., & Washabaugh, P. D. 2005, IJSS, 42, 5322

Kohout, T., Kiuru, R., Montonen, M., et al. 2011, Icar, 212, 697

Marsset, M., DeMeo, F. E., Burt, B., et al. 2022, AJ, 163, 165

National Research Council 2011, Limiting Future Collision Risk to Spacecraft: An Assessment of NASA's Meteoroid and Orbital Debris Programs (Washington, DC: National Academies Press)

Popova, O., Borovička, J., Hartmann, W. K., et al. 2011, M&PS, 46, 1525

Price-Whelan, A. M., Sipőcz, B., Günther, H., et al. 2018, AJ, 156, 123

ReVelle 2006, EM&P, 95, 441

ReVelle, D. 1997, NYASA, 822, 284

ReVelle, D. 2002, in Proc. of Asteroids, Comets, Meteors - ACM 2002, ESA SP-500, ed. B. Warmbein (Noordwijk: ESA), 127

ReVelle, D., & Ceplecha, Z. 2001, in Proc. of the Meteoroids 2001 Conf., ESA SP-495, ed. K. Sweden & B. Warmbein (Noordwijk: ESA), 507

Standish, E. M. 1998, JPL Planetary and Lunar Ephemerides, DE405/LE405, IOM 3312.F-98-048 JPL, ftp://ssd.jpl.nasa.gov/pub/eph/planets/ioms/de405.iom.pdf

Tonry, J. L., Denneau, L., Heinze, A. N., et al. 2018, PASP, 130, 064505

Warner, B. D., Harris, A. W., & Pravec, P. 2009, Icar, 202, 134

Welten, K. C., MEIER, M. M. M., CAFFEE, M. W., et al. 2010, M&PS, 45, 1728

Wright, E. L., Mainzer, A., Masiero, J., Grav, T., & Bauer, J. 2016, AJ, 152, 79